Department of Physics and Astronomy

University of Heidelberg

Bachelor Thesis in Physics

submitted by

Ruth Christine Winter

born in Berlin (Germany)

2018

Low-energy extreme-ultraviolet spectroscopy of Ru IV to Ru VIII using an electron beam ion trap

This Bachelor Thesis has been carried out by Ruth Christine Winter at the
Max Planck Institute for Nuclear Physics in Heidelberg
under the supervision of
Priv.-Doz. Dr. José Ramón Crespo López-Urrutia

Abstract

Astronomical observations of elements heavier than iron in stars are very crucial to understand stellar nucleosynthesis. Elements produced by the slow neutron-capture process, commonly known as the *s*-process, are particularly interesting in that respect because they provide information on the time-scales involved in the process. Ruthenium is among these elements. However, a direct identification of such elements is still not possible since wavelength positions cannot be computed precisely. Therefore, laboratory measurements are crucial to overcome this problem. In this thesis, measurements using an electron beam ion trap device were carried out. Using very low electron beam energies ruthenium ions in the charge states from Ru^{+3} to Ru^{+7} were produced. The fluorescent emitted by these excited ions was recorded using a flat-field grazing incidence spectrometer in a wavelength range of 15 nm to 24 nm. The experimental data unveiled a number of fluorescent lines from ruthenium ions. The line positions and relative intensities were accurately extracted. These data may help to benchmark various theories which further may help to build precise astrophysical models to identify trans-irons lines from the stars.

Zusammenfassung

Astronomische Beobachtungen in Sternen von Elementen schwerer als Eisen sind zum besseren Verständnis der stellaren Nukleosynthese äußerst wichtig. Vor allem interessant sind Elemente, die durch langsamen Neutroneneinfang, bekannt als *s*-Prozess, erzeugt werden. Sie können Informationen über Zeitskalen liefern. Ein Vertreter solcher Elemente ist Ruthenium. Eine direkte Identifikation anhand von spektroskopischen Daten vieler solcher Elemente ist jedoch zurzeit nicht möglich, da die Berechnung ihrer Wellenlängen nicht genau genug ist. Deswegen sind Labormessungen unabdingbar. Die hier vorgestellten Messungen wurden am Max-Planck-Institut für Kernphysik in einer Elektronenstrahl-Ionenfalle durchgeführt. Bei niedrigen Elektronenstrahlenergien wurden Ruthenium Ionen der Ladungsstände Ru^{+3} bis Ru^{+7} erzeugt. Ihre Fluoreszenz wurde mit einem Flachfeld-Weide-Inzidenzspektrometer in einem Wellenlängenbereich von 15 nm bis 24 nm spektroskopiert. Die experimentellen Daten führten zur Entdeckung einer Reihe von Spektrallinien, die Ruthenium Ionen niedriger Ladungszustände zuzuordnen sind. Linienpositionen und relativen Intensitäten wurden mit hoher Genauigkeit bestimmt. Diese Daten können als Vergleich für verschiedenen theoretische Modelle dienen. In Zukunft könnte dies einen Beitrag dazu leisten, genaue astrophysikalische Modelle zu entwickeln, welche die Linienidentifikation dieser Elemente ermöglichen.

Contents

Chapter 1

Motivation

" In the beginning, God created the heavens and the earth. The earth was without form and void, and darkness was over the face of the deep. [...] And God said, "Let there be light," and there was light. [...] And on the seventh day God finished his work that he had done " [Genesis 1, 1-3; 2,2] [1]. Nowadays the idea of the creation of the world is quite different. At the beginning of the universe was the big bang which refers to the starting point of the genesis of matter, space and time. 10^{-35} s after the big bang, the universe consisted of a quark-gluon plasma with a temperature of 10^{28} K [2]. At 10^{-11} s the plasma had cooled down from to 10^{15} K and the leptons were separated up into electrons, neutrinos and their respective antiparticles. Finally after 10^{-10} s at a temperature of 10^{12} K neutrons and protons were formed out of quarks. The density of protons and neutrons was in equilibrium as long as the temperature was high enough [3], through the following reactions.

$$p + e^- \leftrightarrow n + \nu_e \qquad\qquad n + e^+ \leftrightarrow p + \bar{\nu_e} \tag{1.1}$$

1 - 100 s later, the temperature had dropped to 10^9 K. At this point, the electrons did not have sufficient energy anymore to create neutrons from protons through Equation 1.1. Therefore the neutrons started to decay. Only the ones, which had combined with protons into deuterium nuclei remained. This process is called the primordial nucleosynthesis [2].

Approximately 220 s after the big bang at a temperature of $0.9 \cdot 10^9$ K, the density of deuterium nuclei was high enough to form the first helium nuclei and some lithium nuclei. About 3 min after the big bang the nucleosynthesis stopped because no unbounded neutrons were left. The universe cooled down further through its expansion until at a temperature of 3000 K (approximately $4 \cdot 10^5$ s after the big bang) the electrons combined with the nuclei to form the first neutral atom.

All elements heavier than hydrogen and helium, which are nowadays present in the universe had to be formed in stars or supernova explosions. The lighter elements up to iron and nickel were created through nuclear fusion in the cores of stars, a process known as stellar nucleosynthesis. This process becomes ineffective for elements heavier than iron since the energy required for their fusion is higher than the released energy [3].

Elements heavier than iron can be produced by the so-called s-process (slow neutron-capture process) [2]. In this process, the seed nucleus consecutively captures neutrons until it ends up as an unstable isotope. It then undergoes beta decay and becomes a nucleus of the element of the next higher atomic number.

The first evidence that this process takes place in stars was given in 1952 [4]. In spectroscopic observations, the element technetium ($Z = 43$) was detected in the atmospheres of red giant stars. Due to the radioactivity of technetium with a half-life of 210 000 yr, which is much less than the estimated age of red giants, its presence must reflect its recent formation within these stars.

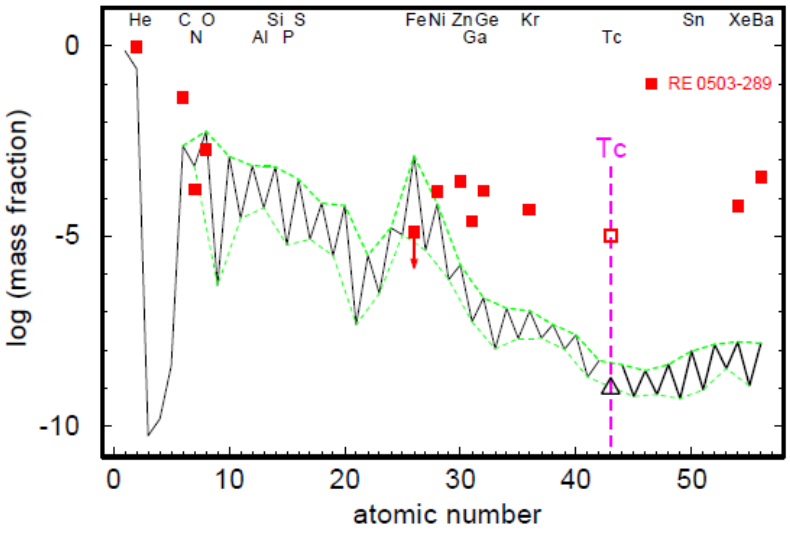

Figure 1.1: Element abundances in *RE 0503-289*, represented by squares, compared to solar values. For technetium the open square marks the detection threshold for *RE 0503-289* and the triangle is the typical abundance in red giants. Taken from [5].

Furthermore, red giants are not the only stars in which atmospheres elements heavier than iron were detected. Another object of particular interest is the white dwarf *RE 0503 - 289*. In its spectrum, as of now, a dozen trans-iron elements have been discovered [6] and there are more lines which have not been seen in any other white dwarf (see Figure 1.1). Presently more than 50 % of these lines are still unidentified, due to the lack of experimental data available for charge states of technetium higher than Tc II. Besides, the line positions, predicted by theory are not accurate enough to allow identifications of observed lines.

In the spectra of *RE 0503-289* charge states of Tc IV-VII are expected in the ultraviolet spectral region. Additionally, laboratory measurements of technetium are challenging due to the radioactivity of this element. Besides the direct measurement of technetium, neighboring elements such as molybdenum and ruthenium can be examined on the premise that their atomic structures are same as of technetium. Whereas data of low charge state of molybdenum is available on NIST [7], atomic data of ruthenium are scarce. Currently no atomic data is available for ions beyond Ru III (see Figure 1.2).

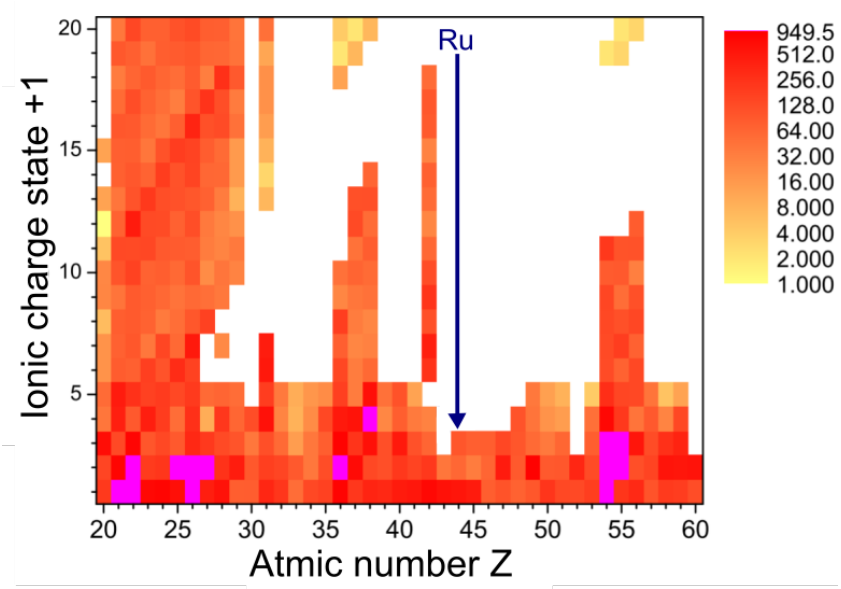

Figure 1.2: Number of spectral transitions known for ions with the atomic number Z and charge state. Adapted from [6].

This thesis works concentrate on measurements of low charge states of ruthenium, mainly Ru IV - Ru IX ions. The measurements are carried out at the FLASH-EBIT located at the Max Planck Insitute for Nuclear Physics. The electron beam ion trap (EBIT) allows to produce, trap and spectroscopically study highly charged ions in one experimental setup. To record the spectra caused by the interaction of ions with a beam of electrons, a flat-field grazing incidence spectrometer, which is able to detect lines in the extreme ultraviolet spectrum, was used. The aim of this work is to provide atomic data for low charge states of ruthenium in a wavelength region from 15 nm to 24 nm. Moreover, charge states of common strong lines in the recorded spectra are identified.

Outline of this thesis

The outline of the thesis is presented in the following:

- Chapter 2: A brief description of the theoretical concepts relevant for this thesis is discussed like the hydrogen atom, selection rules for electronic transitions and atomic processes taking place in an EBIT.
- Chapter 3: The experimental setup is explained in detail, as is the operation principle of an EBIT and the setup of the spectrometer used for detection in the extreme ultraviolet range.
- Chapter 4: Detailed documentation of the parameters used for the measurements.
- Chapter 5: The performed analysis is discussed. Corrections and calibration applied to the measured spectra, analysis for impurities and finally the comparison of the measured spectra with previous ruthenium measurements. The identification of charge states and the comparison with theory are the content of this chapter.
- Chapter 6: Summary and discussion of the results obtained in the previous chapter.

Chapter 2

Theory

An introductory description of some theoretical basics relevant for this thesis is given. Starting with the simplest model of an atomic system, the hydrogen atom, selection rules for electronic transitions are discussed and a brief overview of the important atomic processes which can take place in an Electron Beam Ion Trap (EBIT) is given. A detailed description of the explained concepts is given in [8] and [9].

2.1 The hydrogen atom

The hydrogen atom is one of the simplest atomic systems consisting of only one electron bound to a proton. Therefore, it is a two body system and can be solved analytically. Using the quantum mechanical approach, the entire ensemble can be described completely by its wave function $\psi(t, \mathbf{r})$. This wave function is given by the time-dependent solution of the Schrödinger equation (Formula 2.1).

$$\hat{\mathrm{E}}\psi(t, \mathbf{r}) = \hat{\mathrm{H}}\psi(t, \mathbf{r}) \tag{2.1}$$

Here $\hat{\mathrm{E}} = i\hbar\frac{\partial}{\partial t}$ is the operator for the kinetic energy. The Hamiltonian $\hat{\mathrm{H}}$ is given as

$$\hat{\mathrm{H}} = \frac{\hat{\mathbf{p}}^2}{2m} + V(\hat{\mathbf{r}}) = \frac{-\hbar^2}{2m}\nabla^2 - \frac{Ze^2}{4\pi\epsilon_0 r}. \tag{2.2}$$

The first term takes into account the kinematics of the system and the second describes the coulomb interaction between the proton and the electron whereas $V(\hat{\mathbf{r}})$ is the interaction potential. In this context m is the mass of the electron and e its elementary charge. $r := |\mathbf{r}|$ is the distance between the electron and proton and Z the nuclear charge ($Z = 1$ for the hydrogen atom). $\hbar$ denotes the reduced Planck constant and e_0 the vacuum permittivity.
The spherical symmetry of the systems allows to split the wave function $\psi(t, \mathbf{r})$ into a radial part $R(r)$ and an angular part $Y(\Theta, \Phi)$ which can be expressed by spherical harmonics:

$$\psi(r, \Theta, \Phi) = R(r) \cdot Y(\Theta, \Phi). \tag{2.3}$$

The Schrödinger equation is solved by the eigenvalues E_n depending on the principal quantum number $n \in \mathbb{N}$. The dependence of E_n of n likewise is pointing to the radial quantisation of the energies.

$$E_n = -\frac{m_e e^4 Z^2}{32e_0\ \pi^2\hbar^2 n^2} \tag{2.4}$$

2.2 Selection rules for electronic dipole transitions

When looking at electronic transitions, quantum mechanical selection rules have to be taken into account. If a transition is caused by the absorption of a photon, not only the energy has to be conserved but also the momentum and symmetries of the system. In the following, only electric dipole transitions as the most dominant transition type are considered. In this approximation, the interaction between the light field and the atom is reduced to the interaction between the electric dipole moment of the system with the incoming photon. For a hydrogen atom the electric dipole moment is given by $\mathbf{p} = e \cdot \mathbf{r}$. The transition rate between an initial

state ψ_i and a final state ψ_k depends on the transition dipole matrix element $\mathbf{M}_{ik}$.

$$\mathbf{M}_{ik} = e \int \psi_i^* \mathbf{r} \psi_k dr \tag{2.5}$$

Together the matrix elements $\mathbf{M}_{ik}$ for all possible transitions in an atom form the transition matrix, where all entries different from zero represent allowed transitions in the atom. By evaluating Equation 2.5, one can derive the following criteria for transitions where at least one component is different from zero. This is the condition for a transition to be allowed.
First of all, the magnetic quantum number m_l of the state is considered, which changes by interacting with the angular momentum of the photon. Absorption of a circularly polarized light changes the magnetic quantum number by $\pm$ 1, whereas linearly polarized light, which can be described as a superposition of the two different circular polarizations, leaves the magnetic quantum number unchanged.

$$\Delta m_l = 0, \pm 1 \tag{2.6}$$

Additionally the two wave functions of the states ψ_i and ψ_k should have different parity to guarantee $\mathbf{M}_{ik} \neq 0$. The parity P of a function is defined as even when $f(x) = f(-x)$ and as odd when $f(x) = -f(-x)$. The parity for the wave functions which solve the Schrödinger equation is given by the quantum number l of the orbital angular momentum of the electron as $P = (-1)^l$. This and the condition for the magnetic quantum number m_l given by $-l < m < l$ requires a further selection rule:

$$\Delta l = \pm 1, \tag{2.7}$$

where $l \leq n - 1$ is the quantum number of the orbital angular momentum of the state of the electron.
Each electron has a spin described by the quantum number s which is 1/2 in case of the electron.

The spin is not interacting with the light so for each transition

$$\Delta s = 0 \tag{2.8}$$

is true. The total angular momentum with the the quantum number j given as $|j| = \hbar\sqrt{j(j+1)}$ is the coupling of the spin and the orbital angular momentum. Hence $|l - s| < j < l + s$. The selection rules 2.7 and 2.8 reveal then the selection rule for j:

$$\Delta j = 0, \pm 1. \tag{2.9}$$

Transitions with $j = 0 \leftrightarrow j = 0$ are forbidden.

For systems with more than one electron the total angular momentum given by the quantum number $|J| = \hbar\sqrt{J(J+1)}$ has to be considered. It is again the coupling of the quantum number $S = \sum s$ for the total spin of the system and the quantum number $L = \sum l$ which describes the total orbital angular momentum, hence $|L - S| < J < L + S$. The same selection rules as for single electron transition apply here.

$$\Delta S = 0 \tag{2.10}$$

$$\Delta L = \pm 1 \tag{2.11}$$

$$\Delta J = 0, \pm 1 \tag{2.12}$$

$$\tag{2.13}$$

Transitions with $J = 0 \leftrightarrow J = 0$ are forbidden.

Aside from electrical dipole transitions, there are also higher order contributions to the transition element from multipol transitions e.g. electronic quadrupole transitions and magnetic dipole transitions as the two leading terms. But the corresponding transition rates are usually two to three orders of magnitude smaller than the ones for electrical dipole transitions.

2.3 Atomic processes in an EBIT

In an EBIT, different processes are happening where ions or atoms are interacting with free electrons or photons. To get a better overview, this section is structured into three parts, which describe different types of interactions. In the first part, all processes increasing the charge state of atoms and ions are described, whereas part two discusses processes which decrease the charge state. The third part is dedicated to processes, which produce fluorescence without changing the charge state of the ion for the other processes can produce fluorescence, too. A visual illustration of the various processes discussed is displayed in Figure 2.1

2.3.1 Processes leading to an increased charge state

The most important process which produces highly charge states is **electron impact ionization** (EII) which can occur in interactions of the high energetic electron beam with atoms or ions. A free electron from the beam hits a bound electron from an atom or ion of charge state $q+$ and releases this electron if the kinetic energy of the free electron is greater than the ionization potential I_P of the bound one, creating an ion with charge state $(q+1)+$.

$$A^{q+} + e^-(E_e) \rightarrow A^{(q+1)+} + e^-(E_1) + e^-(E_2) \tag{2.14}$$

The energy difference between the kinetic energy E_e of the incoming electron and the ionization potential I_P is then distributed between the two out coming electrons.

$$E_e - I_P = E_1 + E_2 \tag{2.15}$$

Photoionization is the other process, which contributes to the ion production. It involves an interaction of a bound electron from an atom or ion with a photon γ of energy E_γ greater than the ionization potential of the atom or ion. By absorbing this high energetic photon the

electron is promoted to the continuum.

$$A^{q+} + \gamma(E_\gamma) \rightarrow A^{(q+1)+} + e^-(E_\gamma - I_P) \tag{2.16}$$

2.3.2 Processes limiting the ion production

The two main processes limiting the ion production are recombination processes, in which a free electron is captured into a bound state of an ion. The two most important ones are radiative and dielectronic recombination. Besides charge exchange with residual gas is also reducing the ionization rate in the trap and limiting the highest charge state which can be produced.

During **radiative recombination** (RR) a free electron is captured into a bound state of the ion. The sum of the kinetic energy of the electron and ionziation potential I_P of the state it is captured into, is emitted through a photon.

$$A^{q+} + e^-(E_e) \rightarrow A^{(q-1)+} + \gamma(E_e + I_P) \tag{2.17}$$

Another process is the **dielectronic recombination** (DR) which is a resonant process. Again, a free electron is captured by an ion into a bound state while simultaneously another bound electron is exited to a higher state. This intermediate doubly excited state de-excites by radiative decay.

$$A^{q+} + e^-(E_e) \rightarrow \left[A^{(q-1)+}\right]^{**} \rightarrow A^{(q-1)+} + \gamma(E_\gamma) \tag{2.18}$$

This resonant process takes place only if the condition

$$E_e + I_P = E_{ik} = E_\gamma \tag{2.19}$$

is satisfied. E_{ik} is the energy difference between the initial state i and the excited state k of the bound electron.

In contrast to recombination processes **charge exchange** is an interaction between an atom and an ion, in which the coulomb barrier of the neutral system can be deformed by the close presence of the highly charged ion such that a bound electron from the atom is bound to the highly charge ion after the collision. In general, a highly charged ion A^{q+} interacts with an atom X, mostly light impurity atoms like oxygen or nitrogen, resulting in an electron loss of number k for the light atom and an electron gain of number $p \leq k$ for the highly charged ion, and occasionally a number of free electrons.

$$A^{q+} + X \rightarrow A^{(q-p)+} + X^{k+} + (k-p)e^{-} \tag{2.20}$$

2.3.3 Fluorescence without a change of charge state

The most common process producing fluorescence is **Bremsstrahlung**. A free electron is decelerated by being deflected in the electric field of an ion and emits a photon with an energy equal to the difference in the kinetic energy (initial state i and final state f).

$$A^{q+} + e_{-}(E_i) \rightarrow A^{q+} + e_{-}(E_f) + \gamma(E_i - E_f) \tag{2.21}$$

The last process to be discussed here is **electron impact excitation and deexcitation**. It is similar to electron impact ionization except that the initial energy E_{e_1} of the free electron is not sufficient to release the bound electron. Therefore, the bound electron is excited to a higher state by the collision, producing an exited ion. This decays after a certain time period to a lower level, emitting a characteristic photon, representing the energy difference between the initial state i and the final state k. $E_{e_1} \geq E_{ik}$ must be valid and the energy of the free electron after the collision is stipulated by the energy maintenance, hence $E_{e_1} = E_{e_2} + E_{ik}$.

$$A^{q+} + e_{-}(E_{e_1}) \rightarrow \left[A^{q+}\right]^{*} + e_{-}(E_{e_2}) \rightarrow A^{q+} + e_{-}(E_{e_2}) + \gamma(E_{ik}) \tag{2.22}$$

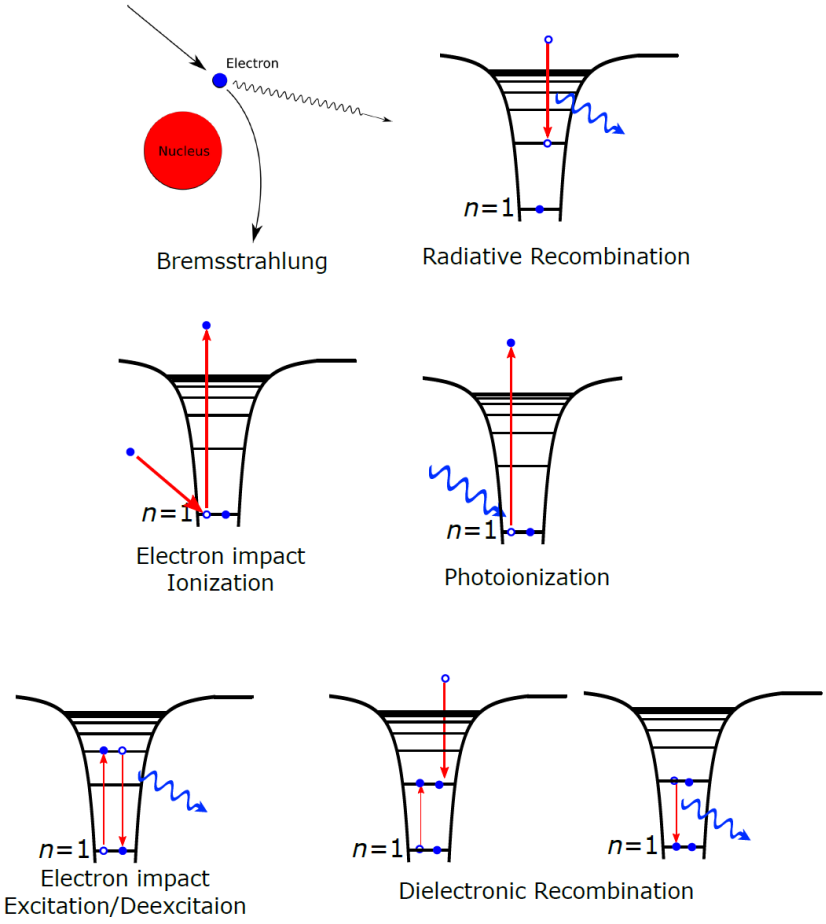

Figure 2.1: Illustration of the atomic processes taking place in an EBIT described in section 2.3. The electron impact ionization and the photoionization are increasing the charge state of an ion, whereas the two recombination processes (radiative and dielectronic) are decreasing the charge state. Bremsstrahlung and electron impact excitation/deexcitation do not lead to a change in the charge state. Adapted from [10]

Chapter 3

Experimental setup

In this chapter, the operation principle of the Electron Beam Ion Trap (EBIT) used in this experiment is discussed including a detailed description of its components [11]. To record these measurements a spectrometer was used, which detects the radiation in the extreme ultraviolet region, hence, the spectrometer is referred to as EUV (extreme ultraviolet) spectrometer in the following. Therefore, the properties of the grating, the detector and a CCD chip used in this setup are explained afterwards.

3.1 The electron beam ion trap (EBIT)

In the electron gun, a high energy electron beam is produced and focused into the trap region where the electrons hit neutral atoms and generate highly charged ions by means of impact ionization. These ions are trapped axially by the electrostatic potentials on the drift tubes and radially by a strong magnetic field as well as by the space charge of the electrons. The electron beam then is guided to the collector where it is dumped.

The EBIT can be divided into three main parts: electron gun, trap, and collector. They are depicted in Figure 3.1 and will be discussed in details in the following.

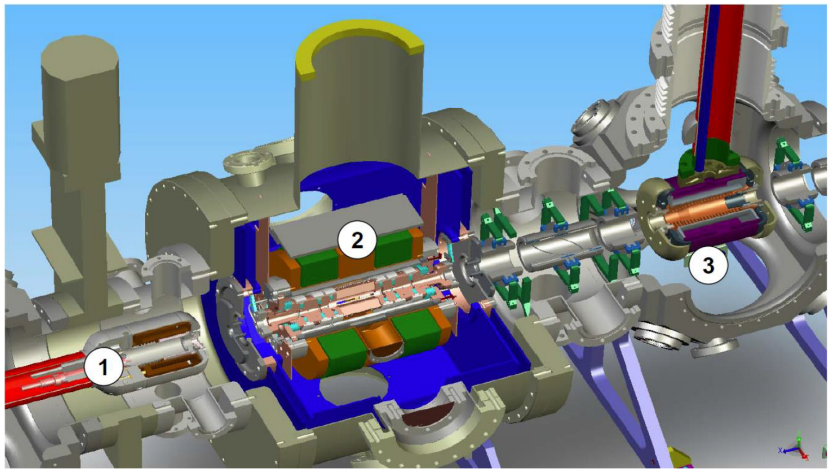

Figure 3.1: This is a sectional view of the EBIT engineering model. The three main parts of the assembly are labelled. (1) the electron gun where the electron beam is produced, (2) the magnet chamber or the trapping region where the ions are produced and trapped, (3) the collector where the beam is finally dumped. Adapted from [12]

3.1.1 Electron gun

The most important part of the electron gun is the cathode, composed of barium and tungsten matrix in this case. Here the electrons are emitted and accelerated towards the trap by applying a positive potential to the anode. The number of electrons per time and impurity ions like tungsten and barium, which are emitted by heating up the cathode, can be regulated by the heating current. The electrons are focused by an electrode, the focus electrode, which is negatively biased and placed in front of the anode (see Figure 3.2). In addition, the focus electrode can be employed quickly to turn off the electron beam in case of an incident by applying a negative voltage with respect to the emission surface so that the electrons cannot pass it anymore. On its way to the trap centre, the electron beam is compressed by a magnetic field of 6 T, produced by a pair of superconducting magnets in Helmholtz coil geometry. For ideal beam conditions, the field on the surface of the cathode has to be zero. Therefore, the magnetic field is counteracted by a magnetic field produced by the trim and bucking coil in the electron gun which can be regulated by applying different currents.

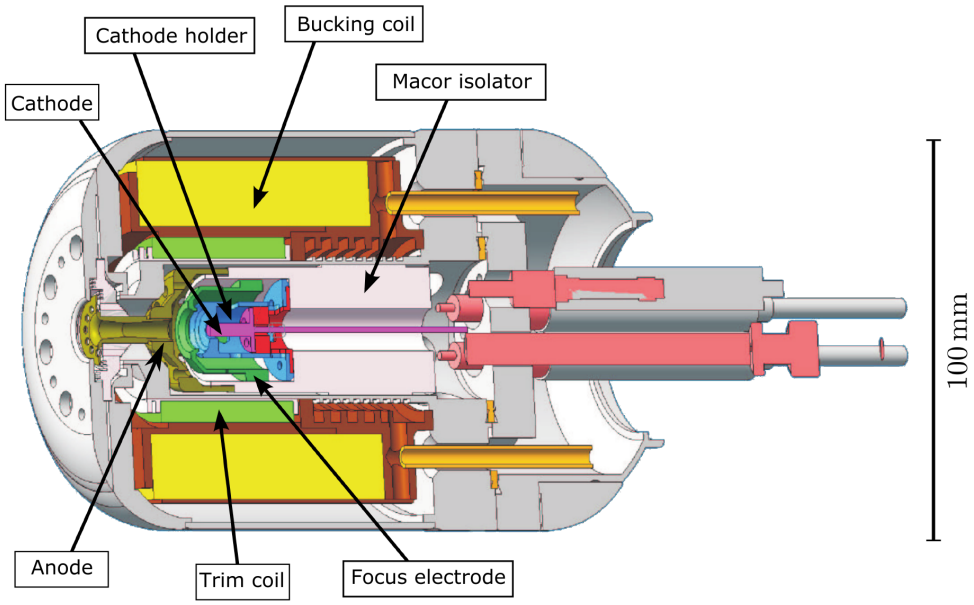

Figure 3.2: Detailed setup of the electron gun. The electrons are emitted from the cathode and accelerated towards the anode while passing the focus electrode. Trim and bucking coil are counteracting the magnetic field from the superconducting magnets to provide a residual magnetic field close to zero for ideal beam conditions. Adapted from [13]

If a laminar flow of the electrons, which means no crossing of the trajectories, and a zero magnetic field at the cathode is assumed, the electron beam radius can be calculated easily like Léon Brillion did in 1945 [14]. Parameters used are the magnetic field strength B at the trap, the electron beam energy E_e, and the electron beam current I_e

$$r_B[\mu\text{m}] = \frac{150}{B}\sqrt{\frac{I_e}{E_e}} \tag{3.1}$$

As this calculation neglects the non-zero temperature kT_c of the electrons emitted by the cathode, it was corrected by Gabriel Herrmann under the assumption that the axial velocity of the electrons is independent of the radial position [15]. It should be been mentioned that this is a semi-empirical approach.

$$r_H[\mu\text{m}] = 260\sqrt{\frac{r_c\sqrt{kT_c}}{B}} \tag{3.2}$$

This formula describes the electron beam radius under ideal conditions where the trim and bucking coils are adjusted to create a residual magnetic field close to zero at the cathode of radius r_c. If one takes into account that the magnetic field is not zero a more complex description of the process is needed which can be looked up in [16]. Approximately, a beam with a radius under 50 µm can be achieved at the FLASH-EBIT.

The total beam energy E_e arises from the potential difference between cathode V_{cathode} and central trap electrode V_{trap} minus the space charge potential $V_{\text{space charge}}$ created by the negative electron beam in the trap. The negative charge of the beam produces negative space charge in a certain reach from the beam which is then reducing the beam energy.

$$E_e = |V_{\text{cathode}}| + |V_{\text{trap}}| + |V_{\text{platform}}| - |V_{\text{space charge}}| \tag{3.3}$$

A last important parameter is the number density of electrons N_e in the beam, which depends on the beam energy E_e and the beam current I_e. This parameter should be constant for different measurements, therefore the beam current has to be adjusted correspondingly for a fixed beam energy. With the velocity of the electrons u at energy E_e given for non-relativistic beams as $u[\text{cm/s}] = 1.9 \cdot 10^9\ \sqrt{E_e}$ a proportional relationship between N_e and the fraction of I_e and E_e can be established.

$$N_e[\text{cm}^{-3}] = \frac{0.8\ I_e}{4\pi {r_H}^2 ue} = 5.9 \cdot 10^{17}\frac{I_e B}{r_c\ u\sqrt{kT_c}} = 3.1 \cdot 10^8 \frac{I_e B}{r_c\sqrt{kT_c E_e}} \propto \frac{I_e}{\sqrt{E_e}} \tag{3.4}$$

3.1.2 Ion trap, drift tubes, and injection system

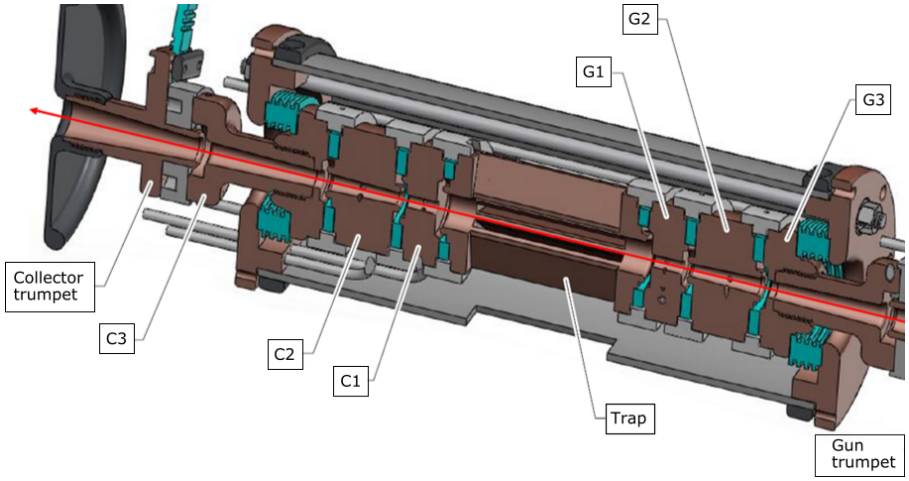

Figure 3.3: Cross section through the drift tube assembly. The drift tubes are labelled similar to their designation in the lab book. The names are referring to the drift tubes on the collector side (C) and the ones on the gun side (G). The red arrow represents the electron beam passing through the set of drift tubes. Adapted from [17]

The trap region consists of nine electrodes, the drift tubes, to which individual potentials can be applied. By choosing suitable voltages, a trapping potential well in the axial direction can be created. Each drift tube can individually be set to a voltage up to 5 kV and the whole assembly can be biased with 30 kV. The arrangement of the electrodes can be gathered from Figure 3.3. At the central drift tube, which is also called trap electrode, the magnetic field is the strongest and most homogeneous. The beam energy of the electron beam is depending on the potential difference between anode and trap minus the space charge (see Equation 3.3). The atoms of interest are injected into the central drift tube through the injection system.

This consists of two stages, first and second injection stage, which are at different vacuum pressures. The source is attached to the first injection stage which is at approximately 10^{-7} mbar. A needle valve is located between the first injection stage and the source. This valve enables to increase the vapour pressure of the source gas and controlling the number of atoms which gets into the injection system. The pressure is then decreased in the second injection to 10^{-9} mbar.

Furthermore, a gate valve between the second stage and the magnet chamber, the injection

valve, can be closed to perform measurements without the source atoms. This enables to detect impurity ions in the trap.

The produced atom beam is impinging on the electron beam to produce highly charged ions by electron impact ionization (EI) as discussed in theory (see section 2.3). The charge states of the ions are depending on many factors, e. g., the electron beam energy and the ionization potentials of the atoms used. The newly produced ions are trapped axially by the potential created by a positive voltage difference applied on the adjacent electrodes. Radially, the ions are trapped by the negative space charge of the electron beam passing through the trap and the homogeneous magnetic field. A further illustration of this process is displayed in Figure 3.4.

Just for trapping, three central electrodes would be sufficient, but the six other electrodes enable different measurement schemes, like producing a longer trap. To do spectroscopy, the trap electrode has eight windows where detectors can be placed to observe atomic transitions in different spectral regimes like EUV (extreme ultraviolet), VUV (vacuum ultraviolet) and X-rays.

For different measurements, the trap depths can be varied to adjust the number density of the ions. In a shallower trap, the ions are cooled down by evaporative cooling effects. Evaporative cooling means that the ions with high kinetic energy escape the trap. Additionally, it is possible to dump the trap contents by increasing the trap voltage for a certain time interval by 500 V to eject ions from the trap.

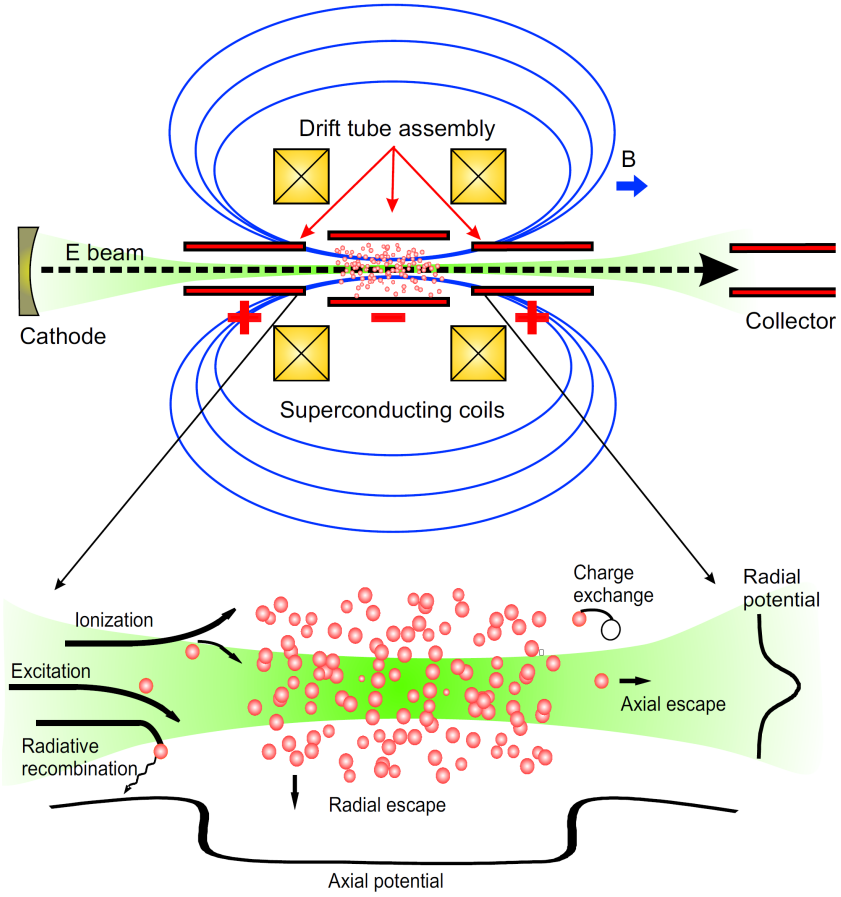

Figure 3.4: The charge breeding and trapping process taking place in the EBIT is illustrated. The ions (red dots) were first ionized by electron impact ionization with the electron beam (shown green) and then trapped axially and radially by the drift tube potential and space charge potential of the electron beam as well as the magnetic field produced by the superconducting coils. [18]

3.1.3 Collector

In the end, the electron beam is caught in the collector. Before the electrons reach to the collector they are decelerated by applying a positive voltage, with respect to the cathode, to the collector. Thus, the collector has to be more negative than the trapping region and more positive than the cathode. Besides, the beam is flared by reducing the magnetic field by means of a magnet coil which counteracts the main magnetic field. To prevent secondary electrons, produced by collision with the collector, from entering the trap region, a slightly negative voltage is applied to the suppressor electrode. The last piece is the extractor, which prevents the electron beam from exiting the EBIT by applying a negative voltage with respect to the cathode.

3.1.4 Vacuum and cooling system

The whole setup is under ultrahigh vacuum (10^{-10} mbar), which is important to reduce the number of ions capturing electrons from background gas atoms and loose consequentially their high charge state. Besides, the emission of unwanted photons from ionized background gas is also limited. The gun assembly is in a vacuum chamber which can be separated by valves to pump it individually. The different spectrometers (EUV, VUV, and X-ray) and the injection system also have gate valves which can be closed. The vacuum system can be seen in Figure 3.5.

Three scroll pumps are used to get the pressure to 10^{-2} mbar, then a $60\,\mathrm{L\,s^{-1}}$ turbo molecular pump serves as fore pump to get the pressure down to 10^{-4} mbar and in the last stage of the pump system the turbo molecular pump of $300\,\mathrm{L\,s^{-1}}$ decreases the pressure to 10^{-9} - 10^{-10} mbar. Besides, electron gun and collector are cooled down by a water chiller to carry away the heat produced in the cathode and by electron collisions.

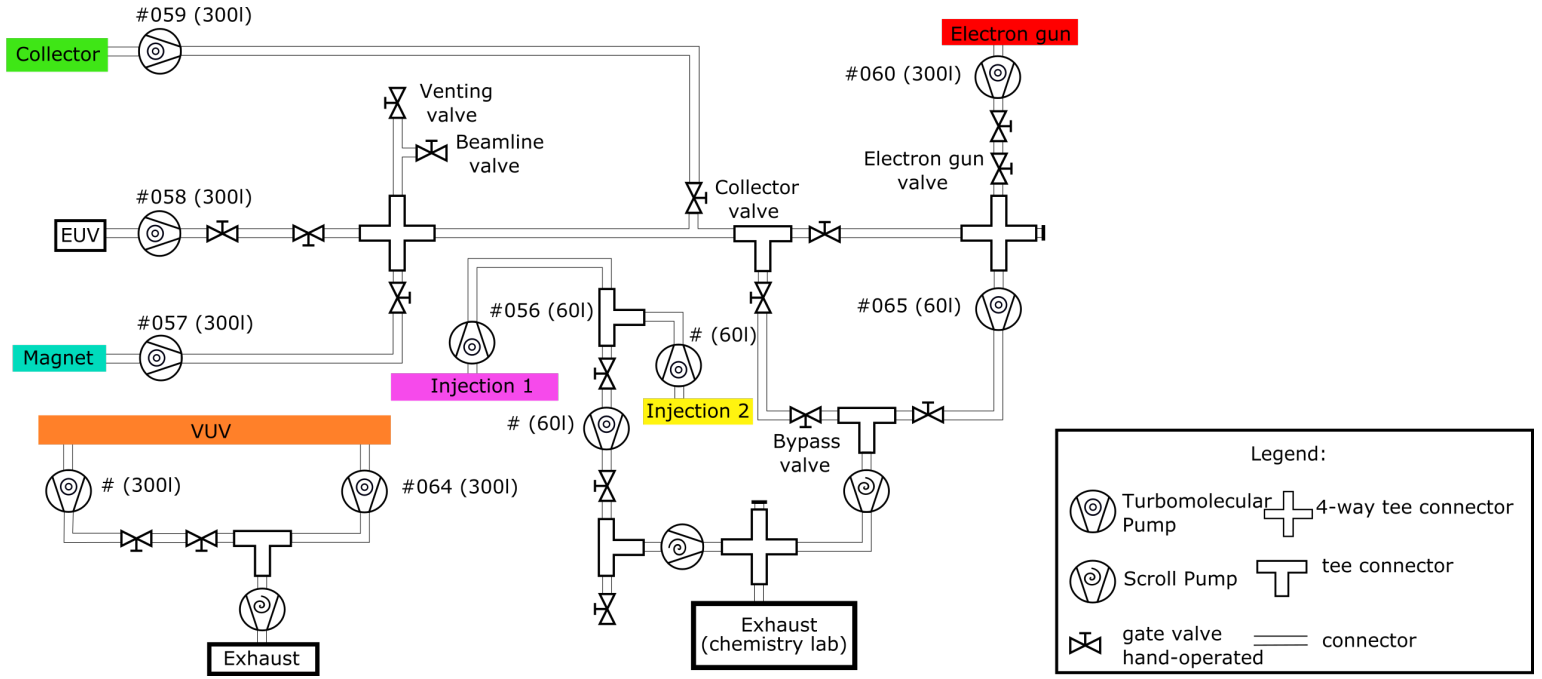

Figure 3.5: Block diagram of the vacuum system of the FLASH-EBIT. All the different pumps and important valves are shown. The colors represent the colors in the pressure diagram in the EBIT control system.

3.2 The extreme ultraviolet spectrometer (EUV)

The measurements in this work were performed at the FLASH-EBIT by means of the extreme ultraviolet (EUV) spectrometer. Consisting of a reflecting, concave grating and a CCD camera for detection of photons, this spectrometer covers a range from 5 nm to 30 nm. It was developed by T. Baumann [19] in 2008 to investigate EUV radiation emitted during atomic processes in an EBIT. In the following, a brief introduction in the qualities of the grating and some information about the characterization of the CCD camera is given.

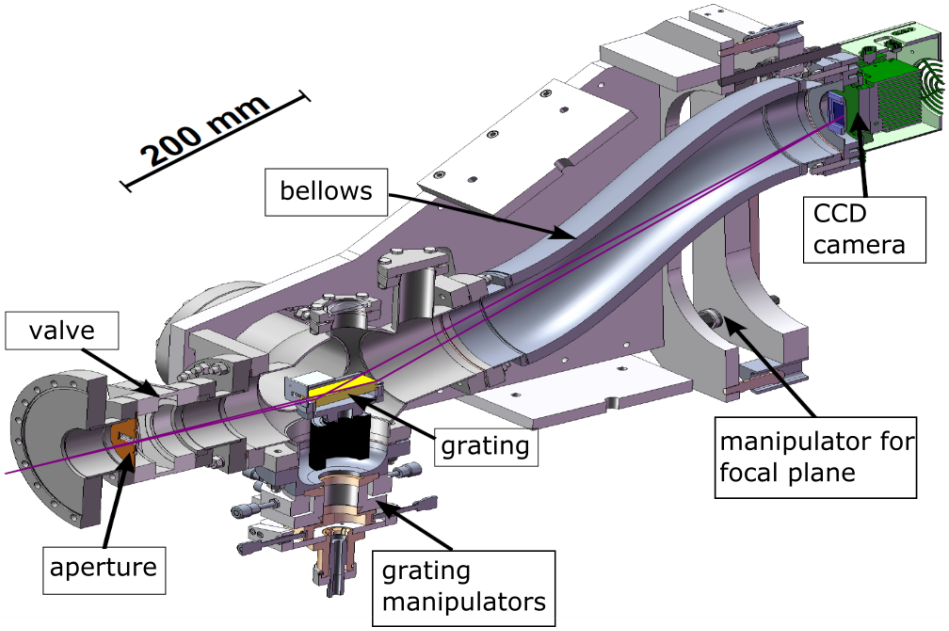

Figure 3.6: Sectional view of the EUV spectrometer with the grating and the CCD camera. Adapted from [19].

3.2.1 Grating

As mentioned before, a reflective, concave grating is employed, which focuses the incoming light emitted during various processes explained in section 2.3, on a focal plane where the CCD camera is placed as photon detector.

The grating installed in the present spectrometer was produced by the company *Hitachi* and consists of gold coated glass. It has 1200 lines per mm with a curvature of 13 450 mm.

To optimize the focusing on the CCD camera multiple parameters can be varied. The grating is mounted onto an adjustment system which enables variation of the grating position in x-, y- and z-direction. The incidence angle α of the light with respect to the grating and the angle of inclination Φ can also be manipulated by this system. Furthermore, the camera height can be adjusted by a linear manipulator. This is needed because the CCD-chip cannot cover the whole spectral range simultaneously and therefore its position has to be changed for observation of the according wavelength.

A small aperture is installed in front of the grating to minimize the side effects of diffuse light and the whole setup is connected to the vacuum of the magnet chamber to prevent the extreme ultraviolet radiation from being absorbed by air. Figure 3.6 shows the setup of the spectrometer.

Table 3.1: grating properties

lines per mm	1200
grating angle α	87°
blaze angle	3°
blaze wavelength	9 nm
diameter R	13 450 mm
distance grating -focal plane y_F	563.2 mm

The grating utilized in this setup is designed for grazing incidence so the angle of incidence α is small. The concave curvature of the grating is decisive for its focusing qualities. The wavelength range where grating reaches maximum reflection is determined by the blaze angle ϑ (parameters see Table 3.1). The grating equation produces of geometric considerations which are illustrated in Figure 3.7.

$$m\lambda = d(\sin\alpha - \sin\beta), \tag{3.5}$$

Where m is the diffraction order and d the groove separation.

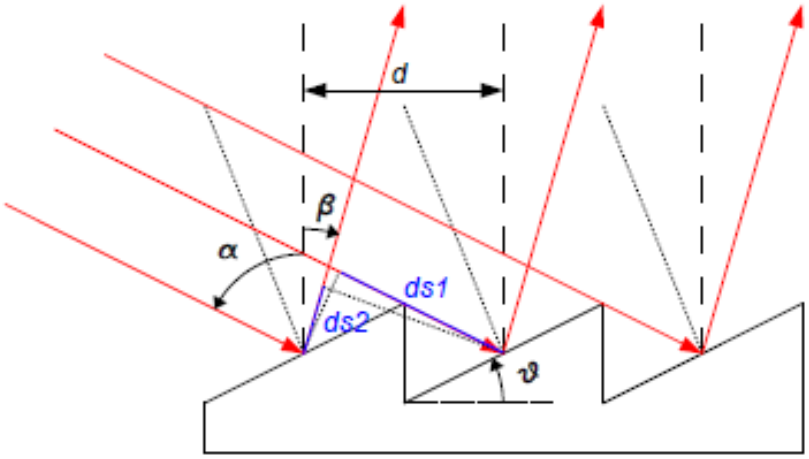

Figure 3.7: Geometrical illustration of the diffraction of incoming light by the grating, adapted from [20]. α and β are the angle of incidence and reflection. ϑ is the blaze angle and the segments marked in blue are relevant to determine the path difference of the light rays.

The grating is a flat-field grating which focuses the incoming light on a the focal plane. This is illustrated in Figure 3.8. The geometric properties give a relation between the vertical position x of the light on the focal plane and y_F which is the distance between the center of the grating and the focal plane.

$$\tan\left(90° - \beta\right) = \frac{x}{y_F} \tag{3.6}$$

The corresponding wavelength to a line position x can now can be calculated with the following Equation by solving Equation 3.6 for β and inserting the result into Formula 3.5.

$$\lambda = d\left[\sin\alpha - \sin\left(90° - \arctan\left(\frac{x}{y_F}\right)\right)\right] \tag{3.7}$$

For calculating the position x, which is needed in 3.7 to calculate the corresponding position in wavelength for a line on the CCD chip, the following parameters have to be measured first: the cameras height position x_{CCD}, the position in pixel x_{pix} of the line of interest on the CCD chip, the camera height position for the zeroth order of diffraction $x_{\mathrm{CCD},0}$, and $x_{\mathrm{pix},0}$ of the line on the CCD chip.

The width b_{CCD} of the effective area of the CCD chip and number of pixels of 2048 are known.

$$x = \frac{x_{\mathrm{pix}}}{2048} \cdot b_{\mathrm{CCD}} + x_{\mathrm{CCD}} - \left(x_{\mathrm{CCD},0} + \frac{x_{\mathrm{Pix},0}}{2048} \cdot b_{\mathrm{CCD}} - x_0\right) \tag{3.8}$$

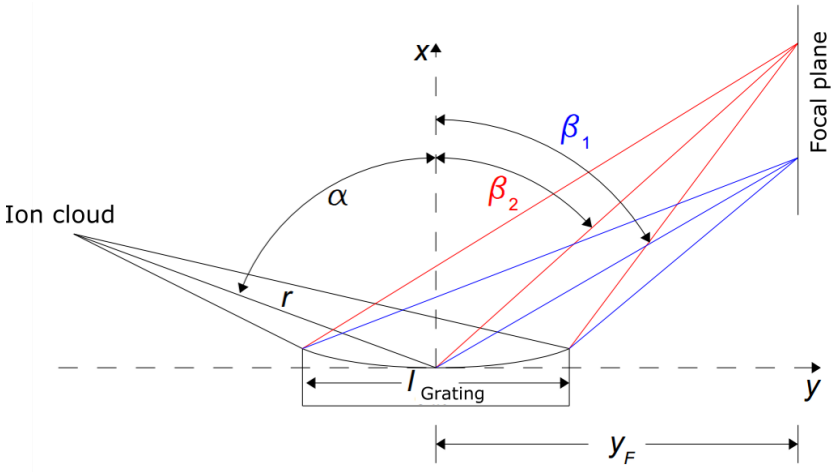

Figure 3.8: Diffraction of the emitted light for two different wavelengths. Adapted from [20].

3.2.2 CCD camera

A CCD camera, hence a charged coupled device is used in this setup to detect the radiation diffracted by the grating. This camera is placed in the focal plane of the grating to get a well focused image. In this setup, a CCD camera of the company *Andor* is used, which also provides the program for the data acquisition *Andor solis*. The heart of the camera is the CCD chip which is divided into 2048×2048 Pixel with an area of 13.5 µm×13.5 µm each, thus the whole CCD chip covers an area of 27.6 mm×27.6 mm.

In the following, the working principle of the CCD chip will be briefly explained.
The CCD chip consists of a semiconductor with an isolating layer. On the isolator are many electrodes, each electrode representing a pixel of the resulting image. The incoming photons transmit their energy through the inner photo-electric effect to the electrons in the semiconductor, which will be transmitted into the conducting band. By applying a positive voltage to the electrodes, the amount of excited electrons, which is proportional to the light intensity, is measured. In the present case, the CCD chip is back-illuminated. This means that the read-out electronics are placed on the backside of the chip which prevents loss of incoming radiation by absorption through the electronic before been detected. The conversion rate of this electronic is 0.7 electrons per count. This describes the number of electrons which are produced by one photon hitting the CCD chip.
A benefit of a CCD measurement is the low signal-to-noise ratio, which is important for a better imaging. Decisive for a high signal-to-noise ratio are mainly two effects. The first noise factor is the dark current which is caused by electrons spontaneously jumping to the valence band due to the thermal energy distribution. The dark current thus is increasing with the exposure time. In this set up the dark current is reduced to a minimum by cooling the device with a Peltier element down to $-70°$ to $-95°$. Secondly, there is the read-out noise, which is independent of the exposure time and comes from the noise generated by the system components, e.g, electronics, and therefore is contributing to each pixel equally when it is read out. By performing a measurement with low exposure time to reduce the effect of the dark current, this effect can be estimated.

Chapter 4

Low energy measurements setup for ruthenium ions

Before starting with data analysis, this chapter will give an overview of how the measurements were carried out and what parameters were selected.

In low energy measurements of ruthenium, the ruthenium source used was the compound Tris(2,2,6,6-tetramethyl-3,5-heptanedionato)ruthenium(III), which is an orange-reddish powder. To get the ruthenium atoms in the trap, the injection system was heated up to approximately 40 - 50 °C. To confirm the presence of ruthenium ions in the trap, measurements at electron beam energies of 280 eV and 360 eV were repeated under similar conditions like in the bachelor thesis of L. Täubert [10]. By comparing the EUV images from the present and the previous measurements it was able to verify the presence of ruthenium. It should be noted that the spectrometer position was changed in between previous measurements of L. Täubert and the present measurement. Due to this fact, camera position was shifted with respect to each other (see Figure 4.1).

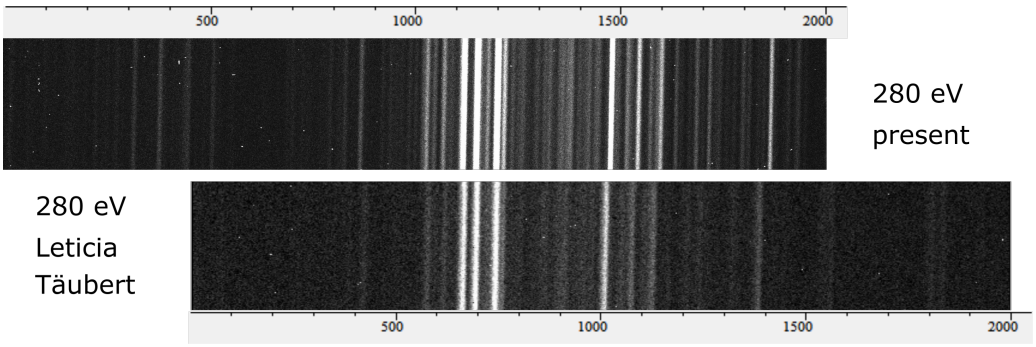

Figure 4.1: The agreement of the lines from the present (above) and previous (below) 280 eV measurement is shown just as the shift in the camera position.

After this verification, the systematic low-energy measurements of ruthenium were started. The energy of the electron beam was chosen by taking into consideration the ionization energies of the different ruthenium charge states (Table 4.1).

Table 4.1: Ionization energies of ruthenium ions in low charge states. The values are taken from [21] and [22]. The electron configuration of the ground state is shown in the last column. The charge state notation is the astronomical one, were the neutral atom corresponds to the roman number I. So Ru II is single ionized Ru.

Charge state	**Charge state**	**Scofield** [eV]	**NIST** [eV]	**Configuration**
0	Ru I	6.4	7.36	$[Kr]4d^7 5s$
+1	Ru II	16.7	16.76 ± 0.06	$[Kr]4d^7$
+2	Ru III	29.4	28.47	$[Kr]4d^6$
+3	Ru IV	43.5	45.0 ± 1.7	$[Kr]4d^5$
+4	Ru V	58.7	59.0 ± 1.9	$[Kr]4d^4$
+5	Ru VI	74.9	76.0 ± 2.0	$[Kr]4d^3$
+6	Ru VII	92.7	93.0 ± 2.0	$[Kr]4d^2$
+7	Ru VIII	110.9	110.0 ± 2.1	$[Kr]4d$
+8	Ru IX	178.5	138.41 ± 0.05	$[Ar]3d^{10}4s^2 4p^6$

The measurements were started at an electron beam energy of 170 eV and continued by reducing the energy untill down to 40 eV to ionize in each measurement a lower charge state from Ru^{8+} down to Ru^{2+} . In Table 4 the parameters for each measurement are summarized. For each measurement the VUV 3m normal incidence spectrometer and the EUV spectrometer, with the CCD camera in kinetic series mode, were running. To detect impurity ions in the trap for each energy a measurement with closed injection was performed. Like one can conclude from Table 4.2 besides the beam energy, the beam current also was adjusted to measure at equal electron beam densities.

The electron beam density N_e is proportional to the ratio of electron beam current I_e and the electron beam energy E_e. So one can calculate the necessary beam current using the previous beam current value I_{e_1} and the electron beam energy of the previous E_{e_1} and the current measurement E_{e_2} by using Formula 3.4.

$$I_{e_2} = I_{e_1}\sqrt{\frac{E_{e_2}}{E_{e_1}}} \tag{4.1}$$

The proportional relationship between the number density of electrons N_e and the fraction of I_e and E_e is used (Equation 3.4). By equating the number densities of the two measurements the proportionally factor cancels out. Solving for the beam current I_{e_2} gives the value which is needed to keep N_e constant for all measurements.

Furthermore, the measurements with beam energies of 55 eV, 72 eV and 90 eV were repeated with optimized trap configurations.

It should also be noted that the potential of the drift tube platform was varied over the measurements and was used to adjust the electron beam energy. This change is due to the low energy measurements which were performed. If the electron beam energy had not be adjusted by the drift tube potential, the electrons would have been ejected too slowly from the gun and would not have gained enough velocity to form a well focused beam. The measurements were started at drift tube platform potential of −150 V for 170 eV, which was then reduced to −215 V for 105 eV, −230 V for 90 eV. Finally setting it to −320 V for 72 eV to decelerate the beam before reaching the trap and thereby reducing the beam energy to the desired one.

Table 4.2: Parameters set during the ruthenium measurements.

E_e [eV]	I_e [mA]	**Trap settings** [V] C trumpet/C3/C2/C1/trap/G1/G2/G3/G trumpet
170	8.7	60/75/75/100/0/100/75/55/30
105	4.5	60/75/75/100/0/100/75/55/30
90	4.1	60/75/75/100/0/100/75/55/30
72	3.0	60/75/75/100/0/100/75/55/30
55	2.2	60/75/75/100/0/100/75/55/30
40	1.1	20/30/30/40/0/40/30/20/10
55	1.8	20/30/30/50/0/50/30/20/10
72	2.6	20/30/30/65/0/65/30/20/10
90	3.8	20/30/30/80/0/80/30/20/10

Table 4.3: EUV data of the ruthenium measurements, yellow marked are analyzed further. For the last measurement at 90 eV a mistake by the designation occurred. Besides it is noted as recorded with closed injection system a comparison proofs it was recorded with an open.

E_e [eV]	**Injection valve**	**Exposure time** [s]	**File name**
360	open	1800	EUV_20180427093618_Ru_15mA_155mm_1_1_0
280	open	1800	EUV_20180427104114_Ru_15mA_155mm_1_2_80
170	open	3600 x 21	EUV_20180428_Ru_15mA_155mm_170eV_kineticSeries
	closed		EUV_20180430_Ru_15mA_155mm_170eV_closed_inj
105	open	3600 x 35	EUV_20180430_Ru_45e-1mA_155mm_105eV_kineticSeries
	closed	3600 x 14	EUV_20180502_Ru_45e-1mA_155mm_105eV_kineticSeries_close_Inj
90	open	3600 x 38	EUV_20180519_Ru_38e-1mA_155mm_90eV_kineticSeries_closedInj
	closed	3600 x 18	EUV_20180504_Ru_45e-1mA_155mm_90eV_kineticSeries_injclosed
	open	3600 x 38	EUV_20180519_Ru_38e-1mA_155mm_90eV_kineticSeries_closedInj
72	open	3600 x 38	EUV_20180517_Ru_26e-1mA_155mm_72eV_kineticSeries
	closed	3600 x 6	EUV_20180517_Ru_26e-1mA_155mm_72eV_kineticSeries_closedInj
	open	3600 x 38	EUV_20180517_Ru_26e-1mA_155mm_72eV_kineticSeries
	closed	3600 x 6	EUV_20180517_Ru_26e-1mA_155mm_72eV_kineticSeries_closedInj

Chapter 5

Data analysis

This chapter gives a detailed description of the analysis of the taken data described in the previous chapter. First, the calibration process is explained, followed by a detailed analysis of the impurities observed in the measurements by comparing spectra taken with open and closed injection. Finally, the examination of the remaining lines for ruthenium and identification of charge states is described.

5.1 Calibration

To analyze the spectra observed with the CCD camera, a calibration with known lines is needed to convert the pixel values into wavelength. Additionally, the lines in the spectra are slightly shifted, which can be observed in Figure 5.1. Therefore, the data is corrected for the shift by using the program *Shift matrix* which shifts vertical slices of the two-dimensional image following a polynomial of the second order to straighten the lines. The parameters for the polynomial set in *Shift matix* were -28 for the first order and -1 for the second order. The data was also corrected for background and cosmics by setting lower and upper limits for the intensity. Afterwards, the data was projected on the horizontal direction by *Shift matrix* to get a final spectrum. The further analyses were carried out in *Origin*, where the *nonlinear fitting function* was used to fit Gaussians to peaks observed in the corrected spectrum.

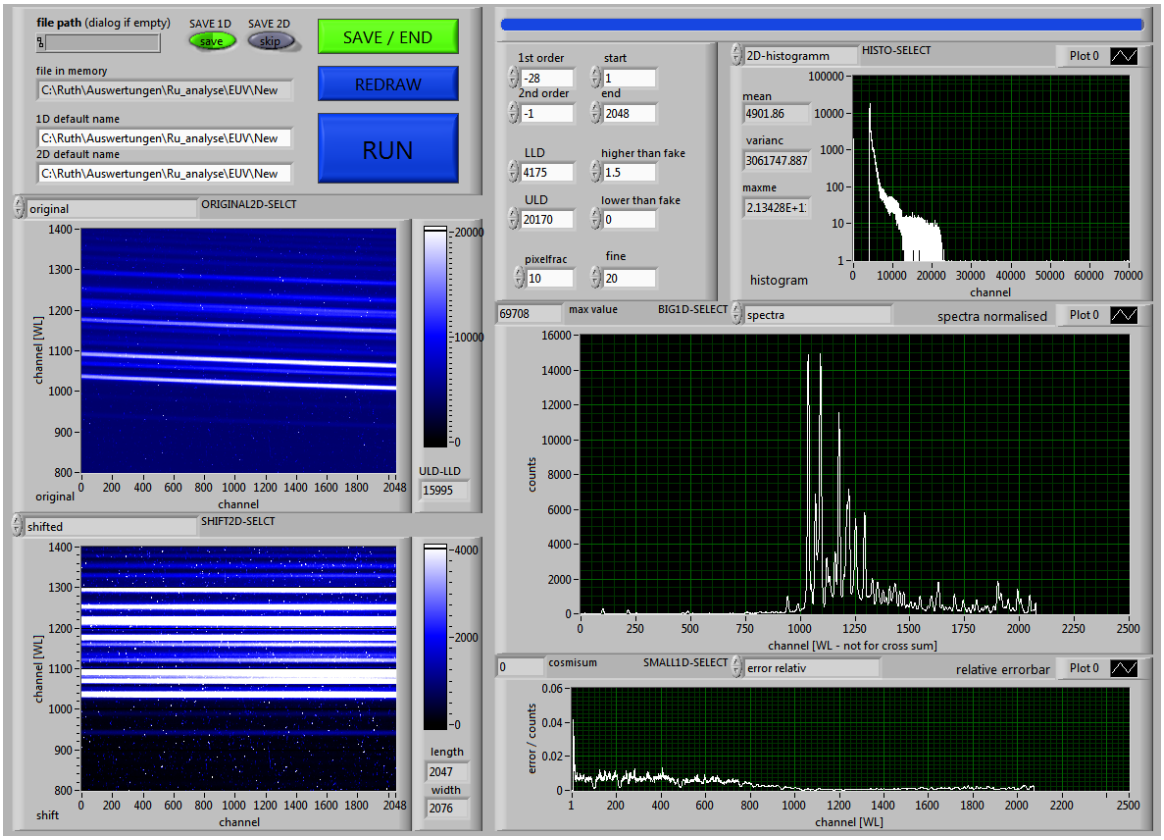

Figure 5.1: Screenshot of the program *Shift matrix*. On the left side, the original spectrum and the corrected spectrum are displayed. One can observe the lines in the corrected spectrum are now quite straight. On the right side the projected spectrum is shown, which was exported as .dat file for the further analysis in *Origin*.

For the calibration, the spectra with the closed injection were used. First of all, a rough calibration is needed to convert the pixel values into wavelength for line identification with literature values. This was done by taken advantage of the analyzed spectra at an electron beam energy of 280 eV and 360 eV from the bachelor thesis of L. Täubert [10]. Common lines in the measurements of L. Täubert and the present measurements were identified. The measured positions in pixel of the identified lines were plotted against the position in wavelength of the lines from L. Täuberts thesis. The identified lines and the corresponding data from L. Täubert are displayed in Table 5.1 and 5.2. Again a polynomial fit was applied to the data by taking into account the uncertainties from the Gaussian fits and the error of wavelengths from L. Täubert. This fit and the corresponding residuals are shown in Figure 5.2. The final values of the fit

parameters are noted down in Table 5.4.

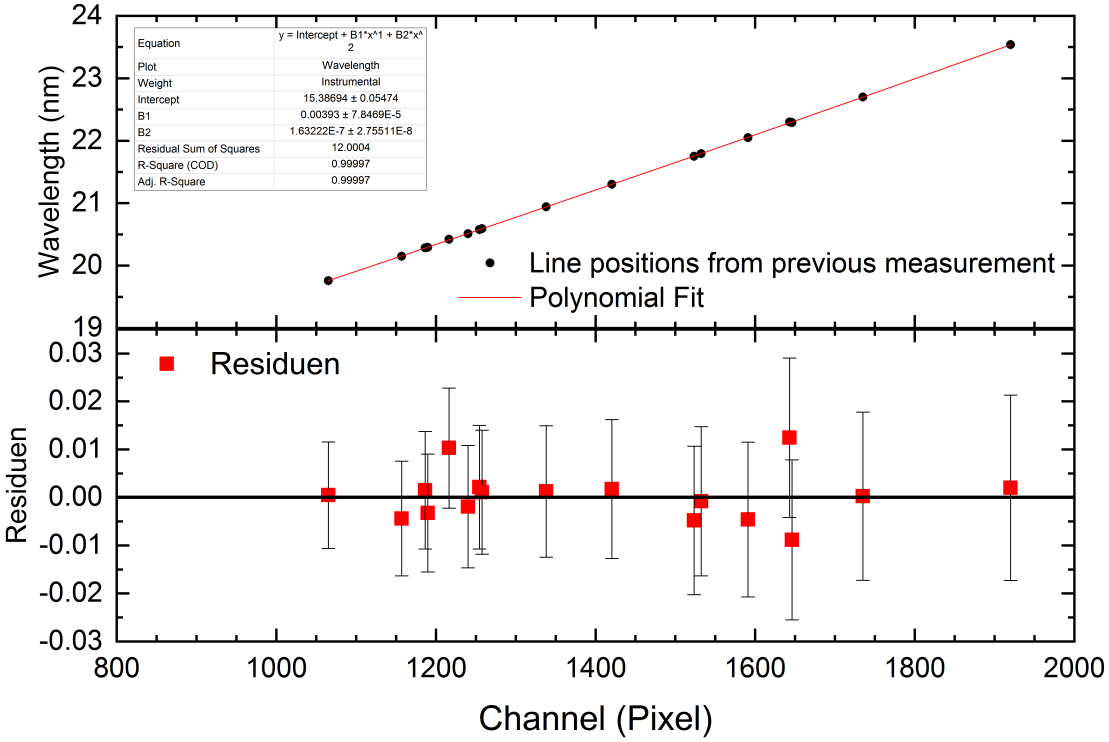

Figure 5.2: Fitting function of the rough calibration with the lines from table 5.1 and 5.2 of L. Täubert measurement at electron beam energies of 280 eV and 360 eV.

Table 5.1: Measured lines in the spectra recorded at 280 eV which were identified with lines in the measurements of L. Täubert [10] for the rough calibration.

Label	**Peak position** [pixel]	**Label** [10]	**Wavelength** [nm]
1	1065.12 ± 0.47	5	19.760 ± 0.004
2	1157.079 ± 0.073	8	20.150 ± 0.004
3	1189.724 ± 0.052	9	20.292 ± 0.004
4	1216.43 ± 0.46	10	20.421 ± 0.005
5	1240.254 ± 0.065	11	20.512 ± 0.005
6	1257.76 ± 0.27	12	20.591 ± 0.005
7	1523.397 ± 0.087	18	21.750 ± 0.006
8	1591.15 ± 0.25	20	22.051 ± 0.007
9	1646.13 ± 0.31	22	22.292 ± 0.007
10	1920.01 ± 0.39	26	23.539 ± 0.009

Table 5.2: Measured lines in the spectra recorded at 360 eV which were identified with lines in the measurements of L. Täubert [10] for the rough calibration.

Label	**Peak position** [pixel]	**Label** [10]	**Wavelength** [nm]
1	1186.54 ± 0.12	3	20.283 ± 0.004
2	1254.53 ± 0.14	4	20.578 ± 0.005
3	1338.09 ± 0.18	7	20.941 ± 0.005
4	1420.37 ± 0.12	8	21.302 ± 0.006
5	1532.425 ± 0.045	9	21.794 ± 0.006
6	1643.17 ± 0.34	10	22.300 ± 0.007
8	1735.112 ± 0.017	12	22.700 ± 0.008

Table 5.3: Ionization potentials of oxygen and nitrogen from the NIST atomic spectra database [21]

Oxygen Z=8	**Ionization energy** [eV]	**Nitrogen** Z = 7	**Ionization energy** [eV]
O I	$13.618\,06 \pm 0.000\,01$	N I	$14.534\,13 \pm 0.000\,04$
O II	$35.121\,12 \pm 0.000\,06$	N II	$29.601\,25 \pm 0.000\,09$
O III	$54.935\,54 \pm 0.000\,12$	N III	$47.445\,30 \pm 0.002\,50$
O IV	$77.413\,50 \pm 0.000\,25$	N IV	$77.473\,50 \pm 0.000\,40$
O V	$113.899\,00 \pm 0.000\,50$	N V	$97.890\,10 \pm 0.000\,40$
O VI	$138.118\,90 \pm 0.002\,10$		

By applying this rough calibration to the carried out measurements at electron beam energies of 170 eV, 105 eV and 90 eV with closed injection observed lines were identified from known spectral lines of oxygen and nitrogen. For that purpose, the atomic spectra database lines form from NIST [7] was used. It is most probable that the lines in the spectra recorded with closed injection belong to oxygen and nitrogen which are prevalent in the atmosphere and consequently the residual gas inside the trap. Especially oxygen has strong lines in the observed wavelength area. Besides, there could be lines from barium and tungsten as these elements are evaporated from the cathode of the electron gun. But in the measured area there are no strong lines of

these elements for the electron beam energies at which the measurements were performed. The relevant ionization potentials of the different elements are listed in Table 5.3. At 170 eV lines from O VII and O VI were expected to be seen in the spectrum. But as there are no lines in the observed area from O VII, only lines from O VI and O V could be identified. The lack of O VII present in the trap is likely due to the space charge of the electron beam which reduces the actual beam energy below the ionization potential of O VII. The lines from O V should be also present in the spectrum taken at electron beam energy of 105 eV and 90 eV. The same should be true for the lines from O IV, which were observed in the spectra recorded at electron beam energy of 105 eV. This information was used to check the validity of the calibration by trying to identify the central wavelength of peaks at same positions (difference in pixel position less than 3 σ). All the identified lines in the spectra can be seen in Tables 5.5, 5.6 and 5.7. The pixel positions and the assigned wavelengths were plotted in a diagram and fitted with a polynomial of the second order using instrumental weighting of the errors (Figure 5.3). The final fit parameters are in Table 5.4.

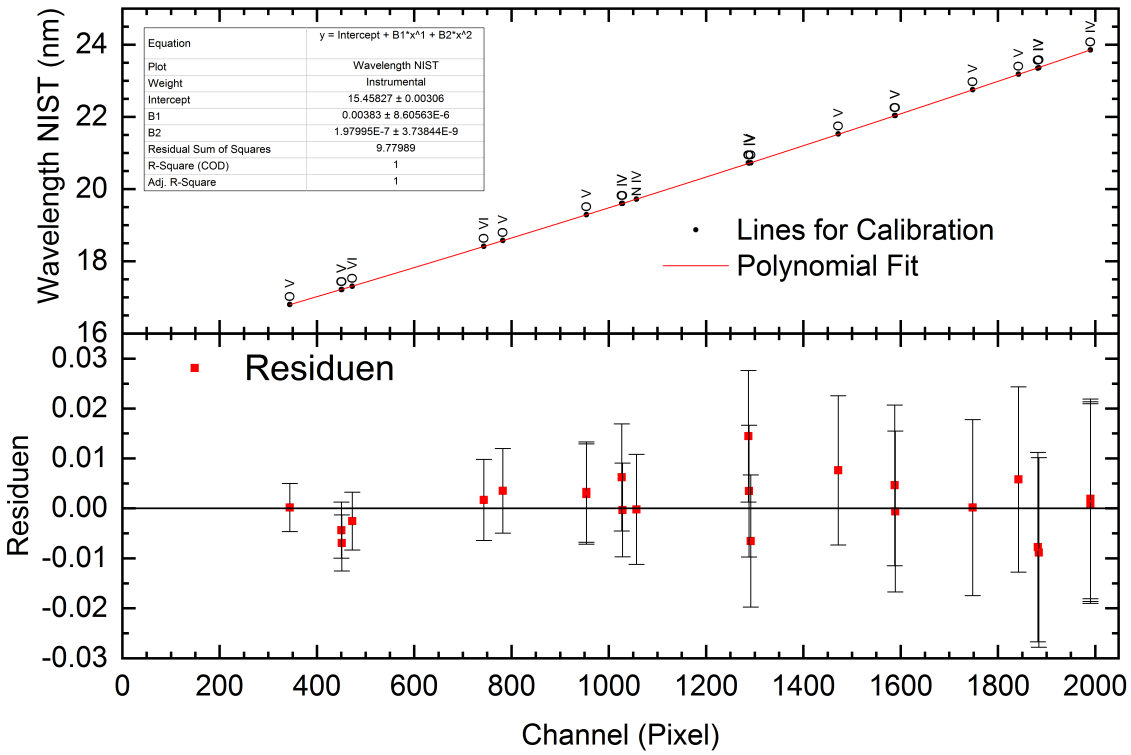

Figure 5.3: Calibration with the lines from table 5.5, 5.6 and 5.7 of the oxygen and nitrogen lines identified in the closed injection from 170 eV, 105 eV and 90 eV

Table 5.4: Fitting parameters all overlapping in 3σ area of the errors

Calibration	**Fitting function:** $y = a + bx + cx^2$		
	a [nm]	b [nm/pixel] 10^{-4}	c [nm/pixel^2] 10^{-7}
280 eV and 360 eV	15.387 ± 0.055	39.30 ± 0.78	1.63 ± 0.28
170 eV - 90 eV	15.4583 ± 0.0031	38.300 ± 0.086	1.980 ± 0.037

Table 5.5: 170 eV with closed injection

Label	**Charge state**	**Configuration**	**Wavelength NIST** [nm]	**Relative intensity**	**Peak position** [pixel]
6	O V	$2s^2 - 2s3p$	17.217 ± 0.023	450	451.02 ± 0.24
7	O VI	$2p - 3d$	17.308 ± 0.005	1000	472.70 ± 0.06
8	O VI	$2p - 3d$	18.412 ± 0.018	850	743.06 ± 0.01
9	O V	$2s2p - 2s3d$	19.291 ± 0.015	520	953.99 ± 0.56
12	O IV	$2s^22p - 2s2p(^3P^0)3p$	20.724 ± 0.100	110	1291.88 ± 0.47
13	O V	$2s2p - 2s3d$	22.035 ± 0.005	520	1588.83 ± 0.34
15	O V	$2p^2 - 2p(^2P^0_{3/2})3d$	23.182 ± 0.008	150	1842.05 ± 1.22
16	O IV	$2p - 3d$	23.857 ± 0.003	180	1990.23 ± 0.75

Table 5.6: 105 eV with closed injection

Label	**Charge state**	**Configuration**	**Wavelength NIST** [nm]	**Relative intensity**	**Peak position** [pixel]
1	O V	$2s2p - 2p(^2P^0)3p$	16.799 ± 0.001	150	344.26 ± 0.39
2	OV	$2s^2 - 2s3p$	17.217 ± 0.023	450	451.02 ± 0.24
3	O V	$2s2p - 2p(^2P^0)3p$	18.575 ± 0.125	250	782.06 ± 0.32
4	O V	$2s2p - 2s3d$	19.291 ± 0.150	520	953.89 ± 0.08
5	O IV	$2p - 4d$	19.601 ± 0.250	200	1026.79 ± 0.55
9	O IV	$2s^22p - 2s2p(^3P^0)3p$	20.718 ± 0.100	150	1288.26 ± 0.29
10	O V	$2s2p - 2s3s$	21.525 ± 0.125	250	1471.72 ± 0.16
11	O V	$2s2p - 2s3d$	22.035 ± 0.005	520	1587.65 ± 0.35
13	O IV	$2s2p^2 - 2s2p(^3P^0)3d$	23.360 ± 1.500	110	1884.20 ± 0.52
14	O IV	$2p - 3d$	23.857 ± 0.003	180	1990.11 ± 0.06

Table 5.7: 90 eV with closed injection

Label	**Charge state**	**Configuration**	**Wavelength NIST** [nm]	**Relative intensity**	**Peak position** [pixel]
1	O IV	$2p - 4d$	19.601 ± 0.250	200	1028.34 ± 0.54
2	N IV	$2s^2 - 2s4p$	19.723 ± 0.075	500	1057.09 ± 0.03
6	O IV	$2s^22p - 2s2p(^3P^0)3p$	20.724 ± 0.100	150	1287.04 ± 0.17
10	O V	$2p^2 - 2p(^2P^0)3s$	22.751 ± 0.003	150	1748.24 ± 0.32
11	O IV	$2s2p^2 - 2s2p(^3P^0)3d$	23.352 ± 0.003	140	1882.24 ± 0.44
12	O IV	$2p - 3d$	23.857 ± 0.003	180	1990.31 ± 0.03

The spectrum with closed injection at electron beam energy of 72 eV was not included in the calibration. At this energy, it was not possible to detect any lines in the spectrum. To Table 5.3 there should be lines from O IV, which were already identified in spectrum at 90 eV because O III does not have any lines in the relevant area. It is assumed that, because of space charge potentials the electron beam energy is reduced and to low to ionize O IV at this beam energy. Nevertheless it is possible that lines from O IV turn up in the open injection measurement with electron beam energy of 72 eV because the total space charge potential is reduced by more positive ions.

The calibration function (parameters see Table 5.4) is applied to all the measured spectra to convert the values in pixel to wavelength in nm. To all peaks Gaussian fits were applied to determine their positions in wavelength. Nevertheless, the same fits with the identical fitting area are executed also in the non calibrated spectra. By this method the peak position in pixel for each peak it obtained which facilitates comparison with previous and future measurements and also, advantageously changes in the calibration can be performed easily. All four spectra with open injection and their measured peaks are shown in the Figures 5.4, 5.5, 5.6, and 5.7, accompanied by Tables (5.8, 5.9, 5.10, 5.11) listing the peak position as well as height, received by the Gaussian fits. The column titled as *Label* corresponds to the numbered, red lines displayed in the figures.
The error for the wavelength was calculated by error propagation to take into consideration the error from the calibration function and the Gaussian fits.

$$\Delta\lambda_{\text{cal}} = \sqrt{(\Delta a)^2 + (x(\Delta b)^2 + (x^2\Delta c)^2 + ((2cx + b)\Delta x)^2} \tag{5.1}$$

Δa, Δb and Δc are the uncertainties of the calibration function which are displayed in Table5.4. x is the peak position and Δx its error in pixel. The error $\Delta\lambda_{\text{fit}}$ resulting from the Gaussian fit in the calibrated has to be added quadratically to this error.

$$\Delta\lambda = \sqrt{\Delta\lambda_{\text{cal}}{}^2 + \Delta\lambda_{\text{fit}}{}^2} \tag{5.2}$$

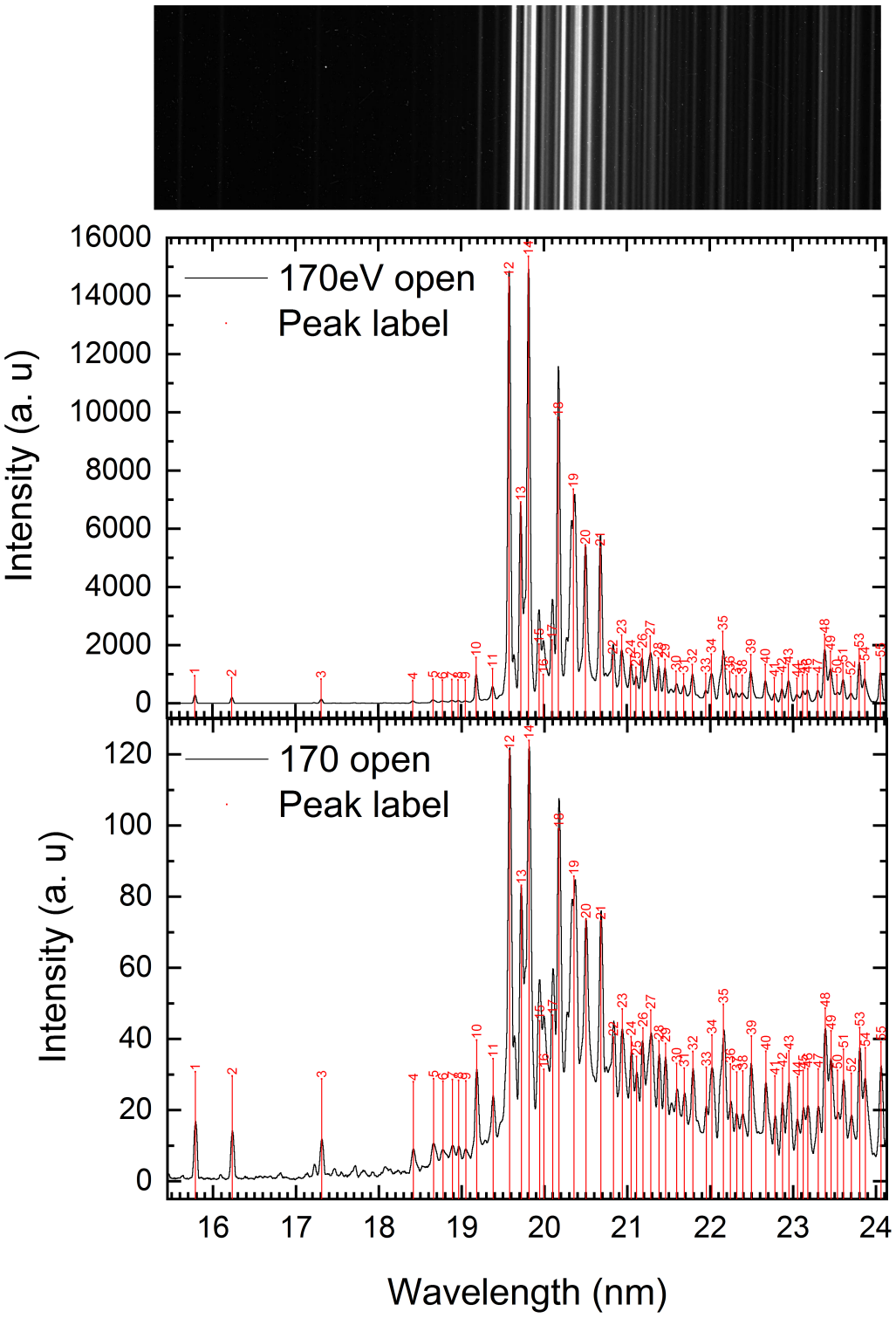

Figure 5.4: Measured spectra at beam energy of 170 eV open injection. The spectra below is plotted with a linear scale on the intensity (below) and spectra above with the square root of the intensities to enable a better differentiation of the smaller peaks from the background. As an illustration the uncorrected CCD image of each energy is displayed over the plotted spectrum.

Table 5.8: Gaussian fitting results of the observed lines for electron beam energy of 170 eV.(L. = peak label)

L.	**Wavelength** [nm]	**Peak position** [pixel]	**Height** [a.u]	**L.**	**Wavelength** [nm]	**Peak position** [pixel]	**Height** [a.u]
1	15.787 (3)	85.50 (10)	249	29	21.462 (15)	1457.69 (41)	801
2	16.232 (4)	199.97 (14)	175	30	21.595 (16)	1487.74 (80)	396
3	17.310 (5)	472.00 (19)	127	31	21.686 (17)	1508.43 (103)	310
4	18.416 (8)	743.74 (30)	81	32	21.792 (16)	1532.23 (49)	631
5	18.661 (8)	803.05 (19)	129	33	21.953 (17)	1568.72 (59)	324
6	18.775 (8)	830.43 (26)	93	34	22.022 (17)	1583.91 (19)	989
7	18.887 (9)	857.17 (21)	116	35	22.159 (17)	1614.66 (10)	1771
8	18.963 (9)	875.40 (24)	104	36	22.244 (18)	1633.76 (49)	384
9	19.050 (9)	896.32 (26)	94	37	22.319 (18)	1650.54 (80)	240
10	19.183 (9)	928.03 (7)	874	38	22.393 (18)	1666.91 (72)	261
11	19.380 (10)	974.80 (13)	485	39	22.496 (18)	1689.94 (19)	968
12	19.580 (10)	1022.05 (10)	13931	40	22.672 (19)	1729.01 (29)	633
13	19.722 (11)	1055.61 (22)	6218	41	22.780 (20)	1752.85 (106)	176
14	19.813 (11)	1077.13 (9)	14660	42	22.872 (20)	1773.07 (60)	312
15	19.943 (14)	1106.58 (55)	1335	43	22.949 (20)	1790.20 (29)	643
16	19.993 (43)	1118.96 (136)	289	44	23.053 (21)	1812.95 (125)	160
17	20.101 (13)	1144.80 (31)	1475	45	23.122 (21)	1828.25 (88)	271
18	20.176 (12)	1161.88 (8)	9119	46	23.178 (21)	1840.41 (75)	301
19	20.356 (12)	1202.87 (21)	6654	47	23.302 (21)	1867.65 (63)	297
20	20.501 (12)	1237.44 (10)	4720	48	23.388 (21)	1886.49 (12)	1667
21	20.681 (13)	1279.11 (10)	4660	49	23.456 (21)	1901.39 (19)	1085
22	20.832 (14)	1313.87 (49)	939	50	23.534 (22)	1918.27 (73)	272
23	20.940 (14)	1338.69 (18)	1642	51	23.606 (22)	1934.05 (28)	674
24	21.045 (14)	1362.65 (39)	950	52	23.701 (23)	1954.71 (85)	221
25	21.111 (15)	1377.74 (75)	527	53	23.804 (23)	1977.07 (17)	1166
26	21.188 (14)	1395.34 (29)	1154	54	23.872 (23)	1991.75 (28)	705
27	21.282 (15)	1416.66 (19)	1613	55	24.060 (23)	2032.38 (22)	835

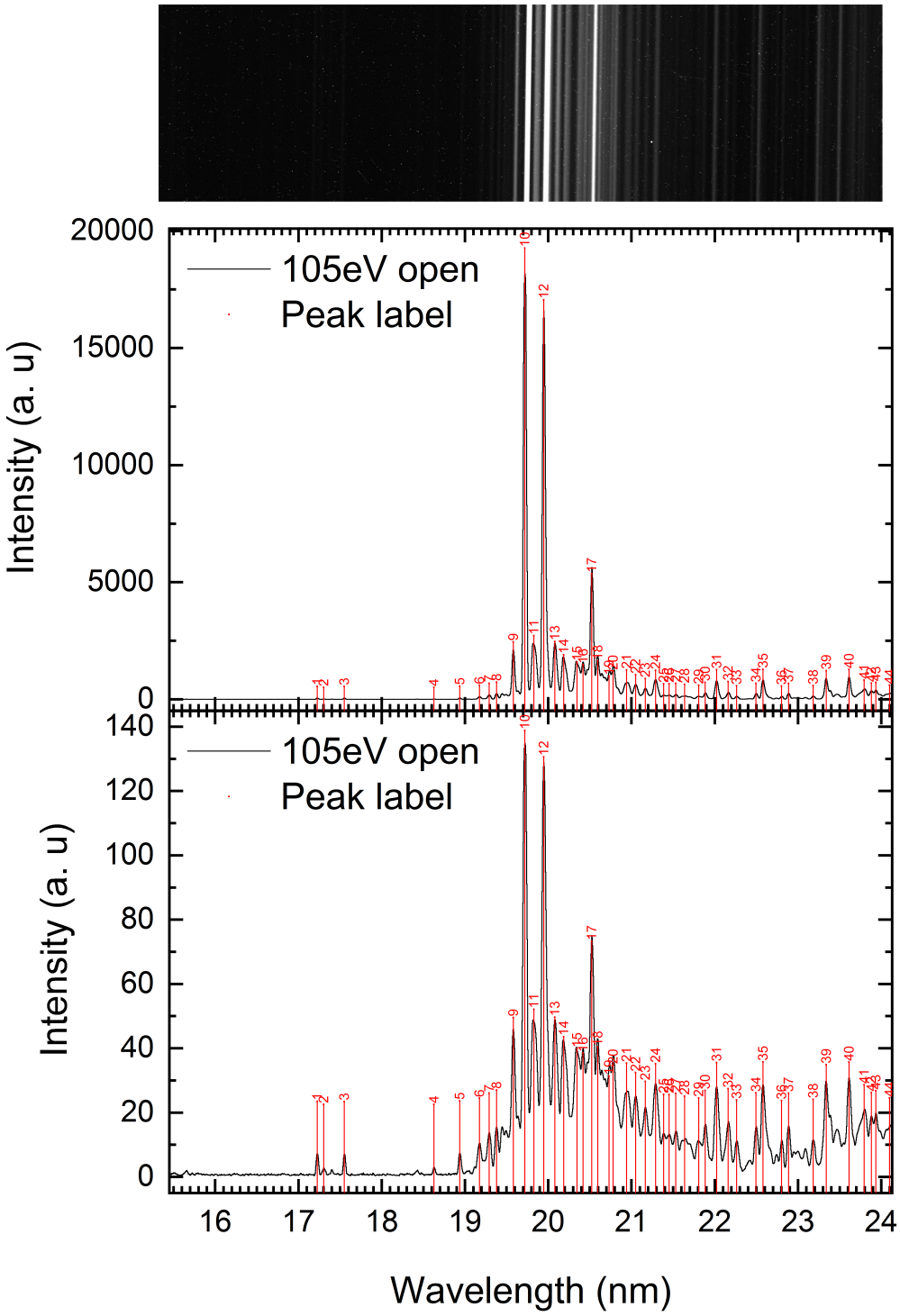

Figure 5.5: Measured spectra of 105 eV open injection. The spectra below is plotted with a linear scale on the intensity (below) and spectra above with the square root of the intensities to enable a better differentiation of the smaller peaks from the background. As an illustration the uncorrected CCD image of each energy is displayed over the plotted spectrum.

Table 5.9: Gaussian fitting results of the observed lines for electron beam energy of 105 eV.

Label	**Wavelength** [nm]	**Peak position** [pixel]	**Height** [a.u]
1	17.225 (5)	450.77 (3)	53
2	17.304 (5)	470.36 (22)	7
3	17.551 (6)	531.71 (3)	50
4	18.627 (8)	794.65 (20)	8
5	18.936 (9)	869.01 (3)	58
6	19.175 (9)	925.98 (18)	100
7	19.290 (9)	953.57 (9)	180
8	19.381 (10)	974.93 (7)	227
9	19.581 (10)	1022.33 (7)	1951
10	19.719 (10)	1054.98 (6)	18766
11	19.828 (11)	1080.48 (46)	2217
12	19.948 (11)	1108.59 (6)	16553
13	20.081 (12)	1139.78 (52)	1967
14	20.187 (12)	1164.49 (74)	1399
15	20.346 (12)	1201.50 (44)	1093
16	20.418 (13)	1218.22 (50)	981
17	20.523 (13)	1242.65 (10)	4863
18	20.596 (13)	1259.34 (44)	1132
19	20.731 (15)	1290.69 (122)	485
20	20.780 (14)	1301.83 (82)	706
21	20.942 (14)	1339.27 (21)	751
22	21.049 (14)	1363.59 (30)	551
23	21.166 (14)	1390.33 (46)	380
24	21.289 (15)	1418.37 (21)	737
25	21.388 (15)	1440.83 (41)	159
26	21.452 (15)	1455.39 (41)	158
27	21.532 (15)	1473.50 (35)	175
28	21.638 (16)	1497.60 (47)	131
29	21.807 (17)	1535.82 (60)	103
30	21.885 (16)	1553.34 (27)	223
31	22.022 (17)	1584.02 (8)	764
32	22.162 (17)	1615.31 (24)	254
33	22.263 (18)	1637.91 (85)	72
34	22.496 (18)	1689.84 (34)	181
35	22.580 (19)	1708.65 (8)	780
36	22.801 (20)	1757.47 (98)	64
37	22.887 (20)	1776.51 (34)	179
38	23.182 (21)	1841.28 (77)	81
39	23.338 (21)	1875.57 (18)	716
40	23.612 (22)	1935.24 (17)	774
41	23.793 (23)	1974.51 (39)	318
42	23.880 (23)	1993.43 (72)	190
43	23.934 (23)	2005.29 (63)	219
44	24.099 (25)	2040.72 (112)	102

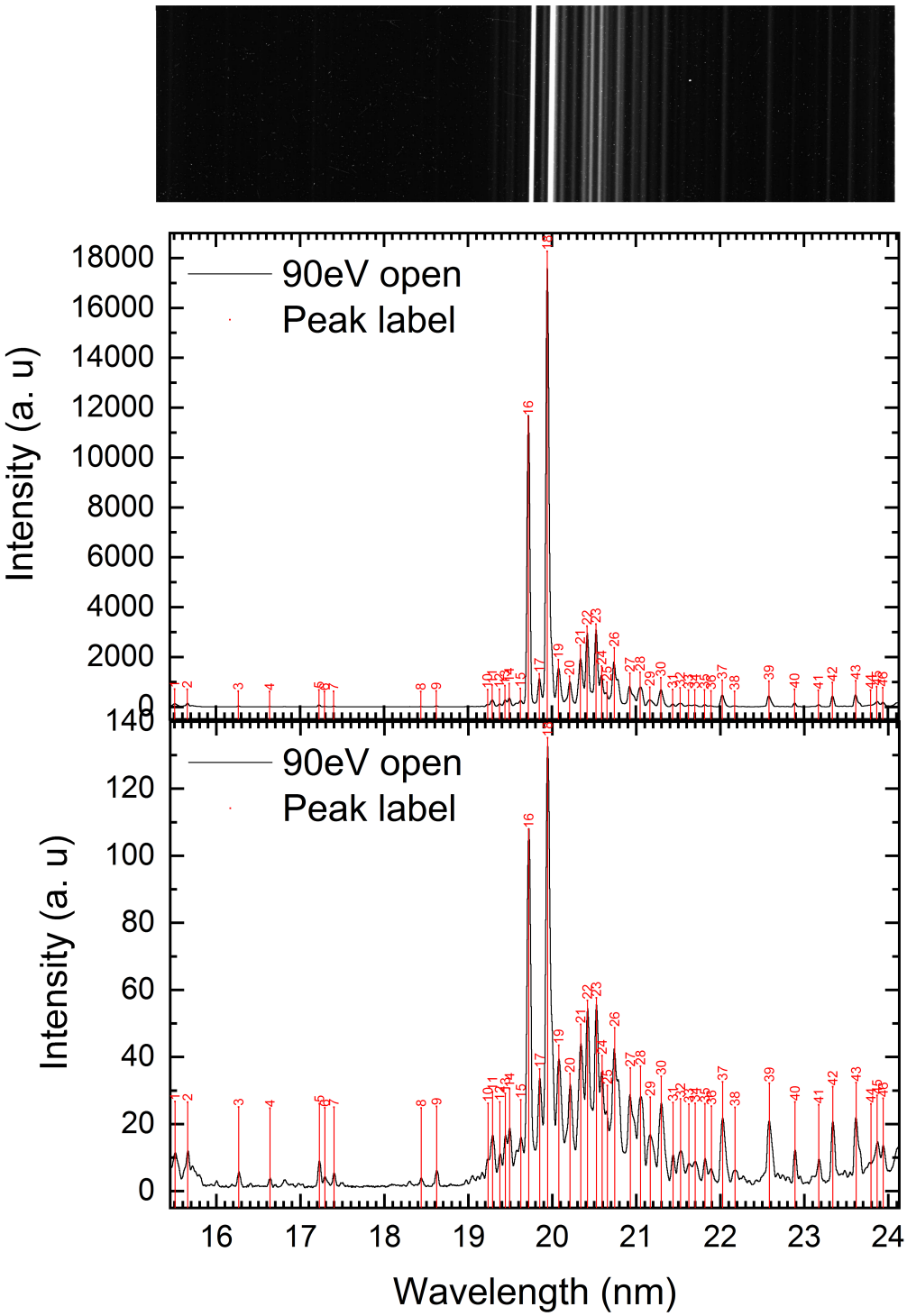

Figure 5.6: Measured spectra of 90 eV open injection. The spectra below is plotted with a linear scale on the intensity (below) and spectra above with the square root of the intensities to enable a better differentiation of the smaller peaks from the background. As an illustration the uncorrected CCD image of each energy is displayed over the plotted spectrum.

Table 5.10: Gaussian fitting results of the observed lines for electron beam energy of 90 eV.

Label	**Wavelength** [nm]	**Peak position** [pixel]	**Height** [a.u]
1	15.509 (3)	13.35 (22)	112
2	15.658 (3)	52.02 (24)	104
3	16.266 (4)	208.73 (10)	29
4	16.637 (4)	302.93 (25)	12
5	17.225 (5)	450.73 (4)	79
6	17.291 (5)	467.27 (18)	17
7	17.400 (5)	494.24 (11)	26
8	18.437 (8)	748.76 (23)	13
9	18.622 (8)	793.39 (8)	37
10	19.233 (9)	940.01 (24)	85
11	19.289 (9)	953.13 (7)	277
12	19.376 (10)	974.03 (17)	108
13	19.442 (10)	989.51 (8)	250
14	19.493 (10)	1001.55 (6)	330
15	19.625 (10)	1032.64 (40)	138
16	19.719 (10)	1055.02 (9)	11038
17	19.851 (14)	1086.07 (138)	723
18	19.946 (11)	1108.14 (6)	17668
19	20.078 (12)	1139.13 (77)	1290
20	20.212 (15)	1170.26 (160)	623
21	20.339 (12)	1199.88 (18)	1871
22	20.420 (12)	1218.72 (12)	2632
23	20.524 (13)	1242.85 (13)	2719
24	20.592 (13)	1258.54 (38)	1029
25	20.656 (14)	1273.38 (93)	390
26	20.744 (13)	1293.57 (18)	1768
27	20.930 (14)	1336.32 (43)	745
28	21.050 (14)	1363.85 (41)	786
29	21.167 (18)	1390.47 (173)	184
30	21.297 (15)	1420.26 (56)	572
31	21.437 (15)	1451.96 (25)	98
32	21.527 (15)	1472.39 (15)	158
33	21.626 (16)	1494.91 (35)	72
34	21.700 (16)	1511.69 (31)	83
35	21.818 (16)	1538.23 (31)	79
36	21.894 (17)	1555.44 (65)	40
37	22.028 (17)	1585.41 (10)	461
38	22.175 (21)	1618.30 (185)	24
39	22.584 (19)	1709.34 (10)	434
40	22.889 (20)	1776.91 (42)	106
41	23.172 (21)	1839.16 (72)	62
42	23.339 (21)	1875.78 (12)	370
43	23.616 (22)	1936.22 (10)	447
44	23.795 (23)	1974.56 (63)	74
45	23.867 (23)	1990.63 (22)	213
46	23.938 (1)	2006.03 (28)	167

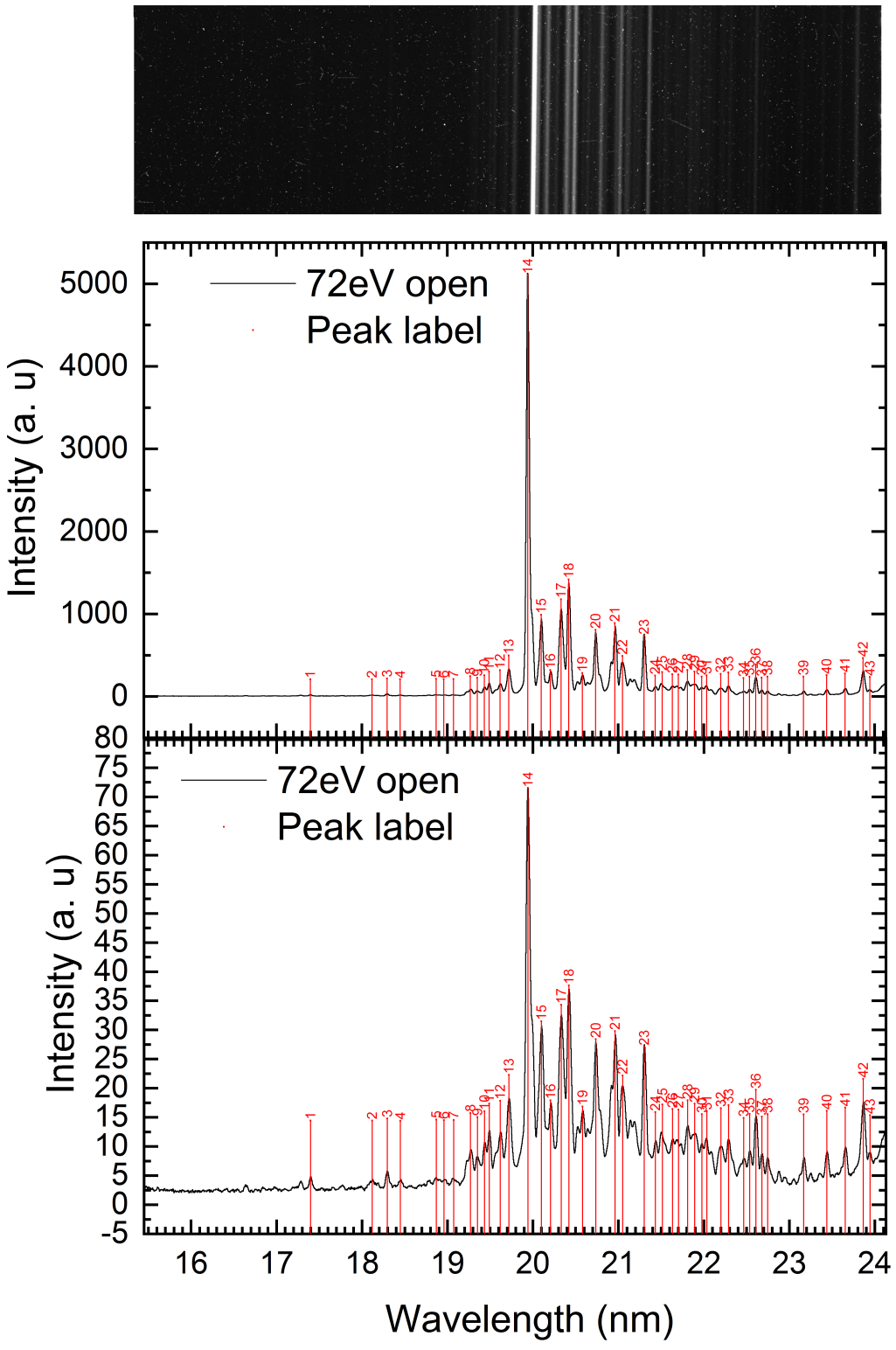

Figure 5.7: Measured spectra of 72 eV open injection. The spectra below is plotted with a linear scale on the intensity (below) and spectra above with the square root of the intensities to enable a better differentiation of the smaller peaks from the background. As an illustration the uncorrected CCD image of each energy is displayed over the plotted spectrum.

Table 5.11: Gaussian fitting results of the observed lines for electron beam energy of 72 eV.

Label	**Wavelength** [nm]	**Peak position** [pixel]	**Height** [a.u]
1	17.397 (7)	493.69 (66)	9
2	18.118 (8)	671.17 (70)	9
3	18.295 (7)	714.34 (32)	19
4	18.446 (9)	751.01 (77)	8
5	18.869 (9)	852.98 (47)	13
6	18.959 (9)	874.45 (60)	10
7	19.072 (9)	901.51 (51)	12
8	19.269 (10)	948.46 (67)	47
9	19.353 (12)	968.42 (125)	26
10	19.433 (11)	987.47 (70)	57
11	19.490 (10)	1000.76 (39)	101
12	19.617 (10)	1030.96 (26)	119
13	19.720 (10)	1055.15 (11)	296
14	19.942 (11)	1107.31 (5)	4906
15	20.099 (12)	1143.98 (31)	790
16	20.206 (17)	1169.06 (204)	121
17	20.333 (12)	1198.40 (25)	977
18	20.421 (12)	1219.00 (20)	1217
19	20.581 (22)	1255.92 (296)	84
20	20.737 (13)	1291.88 (41)	607
21	20.961 (14)	1343.40 (36)	689
22	21.051 (15)	1363.96 (85)	291
23	21.303 (15)	1421.52 (46)	536
24	21.432 (16)	1450.97 (70)	53
25	21.515 (15)	1469.60 (36)	96
26	21.633 (16)	1496.37 (56)	70
27	21.704 (16)	1512.54 (58)	66
28	21.811 (16)	1536.54 (29)	122
29	21.892 (17)	1554.78 (42)	101
30	21.977 (19)	1573.96 (143)	42
31	22.036 (18)	1587.09 (98)	57
32	22.198 (17)	1623.54 (27)	75
33	22.289 (18)	1643.78 (22)	92
34	22.465 (19)	1682.98 (91)	23
35	22.536 (19)	1698.67 (49)	42
36	22.608 (19)	1714.84 (11)	190
37	22.678 (19)	1730.36 (74)	28
38	22.746 (19)	1745.33 (27)	41
39	23.168 (20)	1838.23 (28)	40
40	23.439 (21)	1897.61 (19)	59
41	23.653 (22)	1944.29 (14)	78
42	23.863 (23)	1989.85 (5)	267
43	23.943 (23)	2007.00 (35)	36

5.2 Investigation of ruthenium lines

This part of the chapter is focused on the examination of the measured spectra for ruthenium lines. First, lines originating from impurities are excluded by a detailed analysis, then the measurements are compared with previous measurements from J. Jäger [23]. Common strong lines of the spectra are examined for their charge states. Finally, the data is compared with a collisional radiative model for Ru^{5+} and Ru^{6+}.

5.2.1 Comparison between open and closed injection measurements

Before starting to check for possible ruthenium lines, first all the lines had to be filtered out, which originate from other ions like oxygen, nitrogen, barium, and tungsten. Lines from oxygen and nitrogen were already identified in the measurements with closed injection and these lines are expected to turn up again in measurements with open injection.

Therefore, a comparison between the open and close injection is helpful. In Figure 5.8, spectra with and without closed injection are plotted in one graph for the measured electron beam energies at 170 eV, 105 eV, 90 eV and 72 eV. The drop lines correspond to the peak label at the peak centroid position. The y-axis represents the square root of the intensities. Naturally, the closed injection spectra have lower intensities than those measured with the injection opened so that a comparison without nonlinear scaling is difficult. Additionally, the intensities of the measurement with closed injection are normalized to be similar to the intensities measured with open injection. This was done by identifying one peak of the closed injection in the open one, like a strong O VI line, and then multiplying the intensity ratio from open and closed injection of this peak to the intensities of the closed one. This was done for all three spectra individually. In each spectrum, the peak with the highest intensity in the measurement with closed injection was selected for this normalization under the assumption that it could be re-identified in the measurement of the open injection.

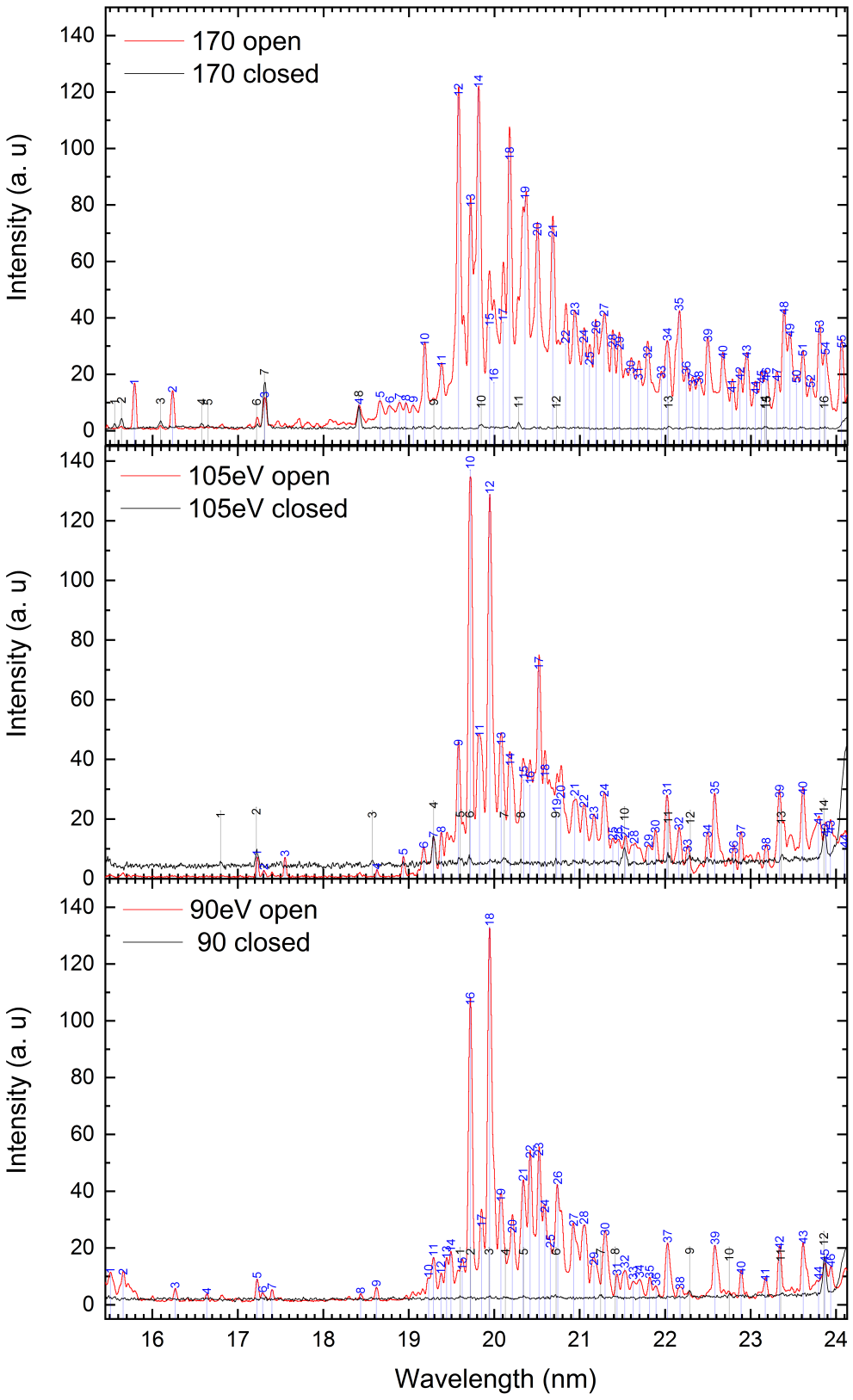

Figure 5.8: A comparison between open and closed injection for the measurement at beam energy of 90 eV, 105 eV and 170 eV. On the y-axis, the square root of the intensities is plotted against the wavelength. The closed injection measurements are normalized to the open one for better comparison.

5.2.2 Detailed analysis of the impurities

A detailed analysis of the impurities visible in the spectra was performed. This is important to prevent misidentification of potential ruthenium lines. The wavelengths obtained with the Gaussian fits from the measurement at open injection at beam energies from 170 eV to 72 eVwere compared with literature values. The literature values of observed and Ritz wavelengths were from NIST [7] and [24] of oxygen, nitrogen, barium, and tungsten in the appropriate charge states were taken.

To exclude mistakes during this complex identification process simulated spectra produced by the NIST database were used and compared with the measurements. So when a strong line from one charge state was identified, the others lines from this charge stare were also expected to appear. Likewise, when from one charge state only one matching line was found, it was less probable that the assignation was true when other lines from this charge state were not appearing in the measurements. Attention was paid that the intensities of the measured spectra and the identified lines are in agreement.

If literature value (from NIST) and experimental one were matching in the 3 σ area of their errors an assignment was taken for correct. By comparing the measured wavelengths within their errors common lines in the different measurements were identified. All the measured lines, their identified element, its charge state and configuration, as well as the literature values and the difference between experiments and literature values can be seen in Tables 1, 2, 3 and 4 in the appendix. All identified impurities are added to the spectra in Figure 5.9 and 5.10. The y-axis in this plots presents the intensity of the measured spectrum and the relative intensity of the identified transitions, normalized as described before. Again a line with the strongest intensity identified in the closed injection which also reappeared in the open injection was used to normalize the relative intensities from NIST to the intensity value measured for this line. Hence, NIST intensities were multiplied by the ratio of measured intensity and the literature intensity.

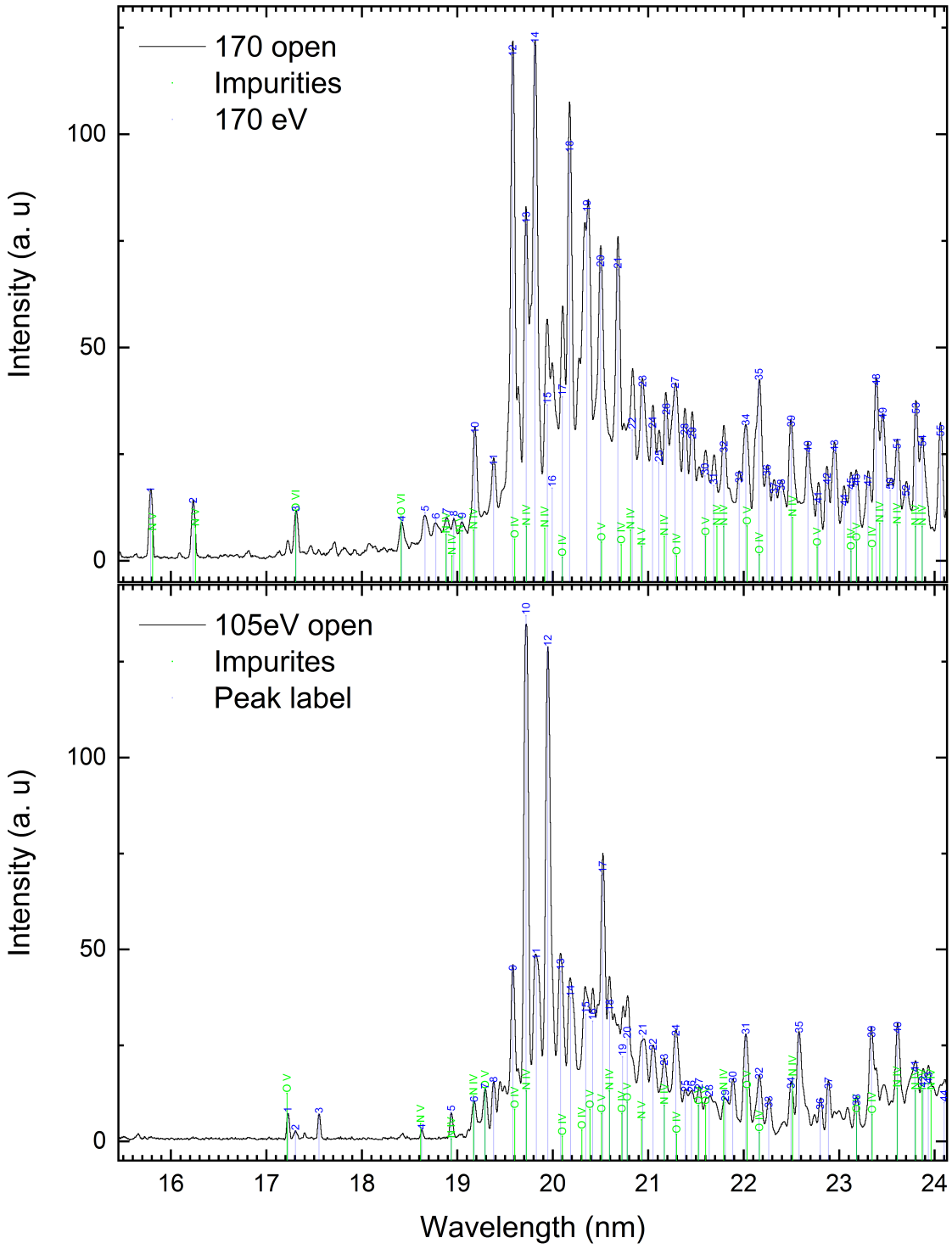

Figure 5.9: Assigned impurities in the open injection from 170 eV and 105 eV. The relative intensities from the impurity lines are normalized to the measured intensities by using a strong line from the closed injection which was also present in the open injection. Details for the identified lines are in Table 1 and 2.

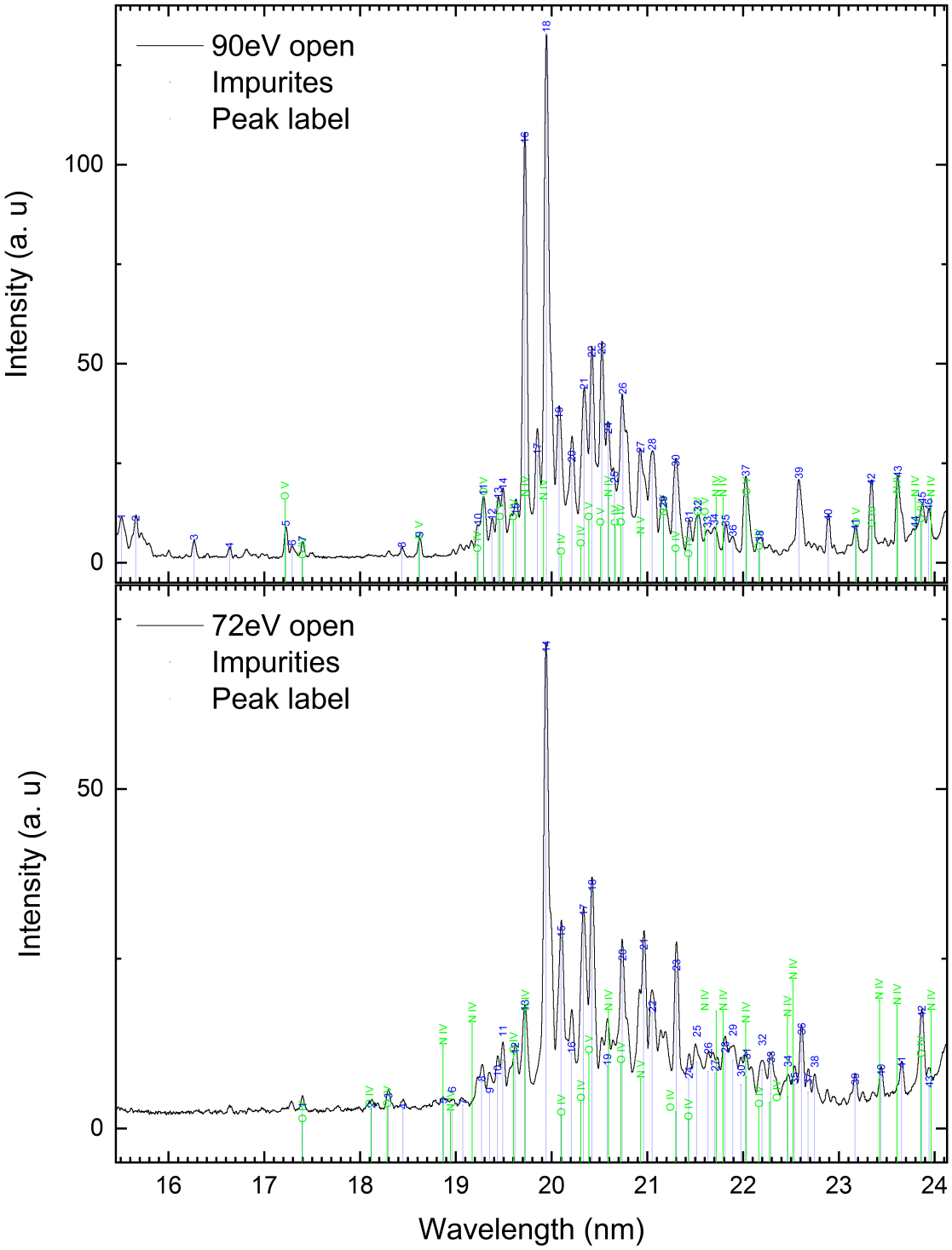

Figure 5.10: Assigned impurities in the open injection from 90 eV and 72 eV. The relative intensities from the impurity lines are normalized to the measured intensities by using a strong line from the closed injection which was also present in the open injection. Details for the identified lines are in Table 3 and 4.

In this way, it is easier to get an impression of the contributions of impurities to the measurement. From the Figures 5.9 and 5.10 can be concluded that these contributions are not significant. As can be seen, there are some weak lines at the low and high wavelength ends of the spectra. There are also some weak impurity lines which may be contributing to the lines of strong intensity in the middle of the spectra. However, their intensities are too weak to cause the strong lines which were measured at these positions. Mainly the impurities are contributing to the background. Also, the conclusion can be drawn that only low charge states of oxygen and nitrogen are relevant. These are frequent gases in the atmosphere and oxygen is also contributed by the organometallic component used as Ruthenium source in the injection system. Carbon is also contained in this composition but no strong lines of this element were observed, so it is not relevantly contributing to the measurements.
This analysis shows also that the spectra are free from iron lines, which are often present because iron is difficult to remove from the trap but used for calibration due to its well-known lines.

5.2.3 Comparison with previous ruthenium measurements

In the context of this thesis, it is also interesting to compare the measured spectra with previous ruthenium measurements carried out at the FLASH-EBIT with the EUV spectrometer under similar conditions. The present data are compared with the data taken by J. Jäger in 2017 [23] with an electron beam energy from 100 eV to 230 eV.
So the present measurements expand this series even further down to lower electron beam energies. This is illustrated by the following Figure 5.11. All intensities were normalized by the *normalize [1,0]* function of *Origin* to ease comparison. Again the square root of the intensities is plotted at the y-axis to enhance the visibility of the smaller peaks. In the Figure 5.11 different peaks are appearing and fading over the energy range from 72 eV to 170 eV which indicates the production of different charge states. Besides measurements were optimized which results in higher intensities and more observed lines which can be seen in the comparison of spectra from 150 eV to 170 eV. They are plotted in Figure 5.12. From this comparison it is concluded that

the present measured spectra at electron beam energy of 170 eV has an lower actual energy than the old one because two strong peaks from the old 170 eV measurement are not appearing in the present measurement at the suspected same electron beam energy. On the other hand the two strong lines which are present in the the old 160 eV and 150 eV measurement are in agreement with the new measurement at 170 eV. However the present lines seem to be stronger which can be an effect of the improved intensity of the measurement and a different energy even lower than the for the old measurement at 150 eV. This impression is reinforced by the closer examination of a line appearing between the two strong lines in the measurement at 150 eV. This line is stronger in the present measurement at 170 eV than in the old one at 150 eV. Also other lines seem to have gained intensity. This is a strong argument for the present 170 eV spectrum having been taken at real energy below the one of the previous 150 eV measurement. The different energy is most likely a result of a different space charge influence due to different measurement conditions, e.g., the electron current and number density of ions.

Finally, it should be remarked by this comparison that the calibration could also be confirmed because the strong lines are appearing at the same wavelength positions and are not showing any significant deviation.

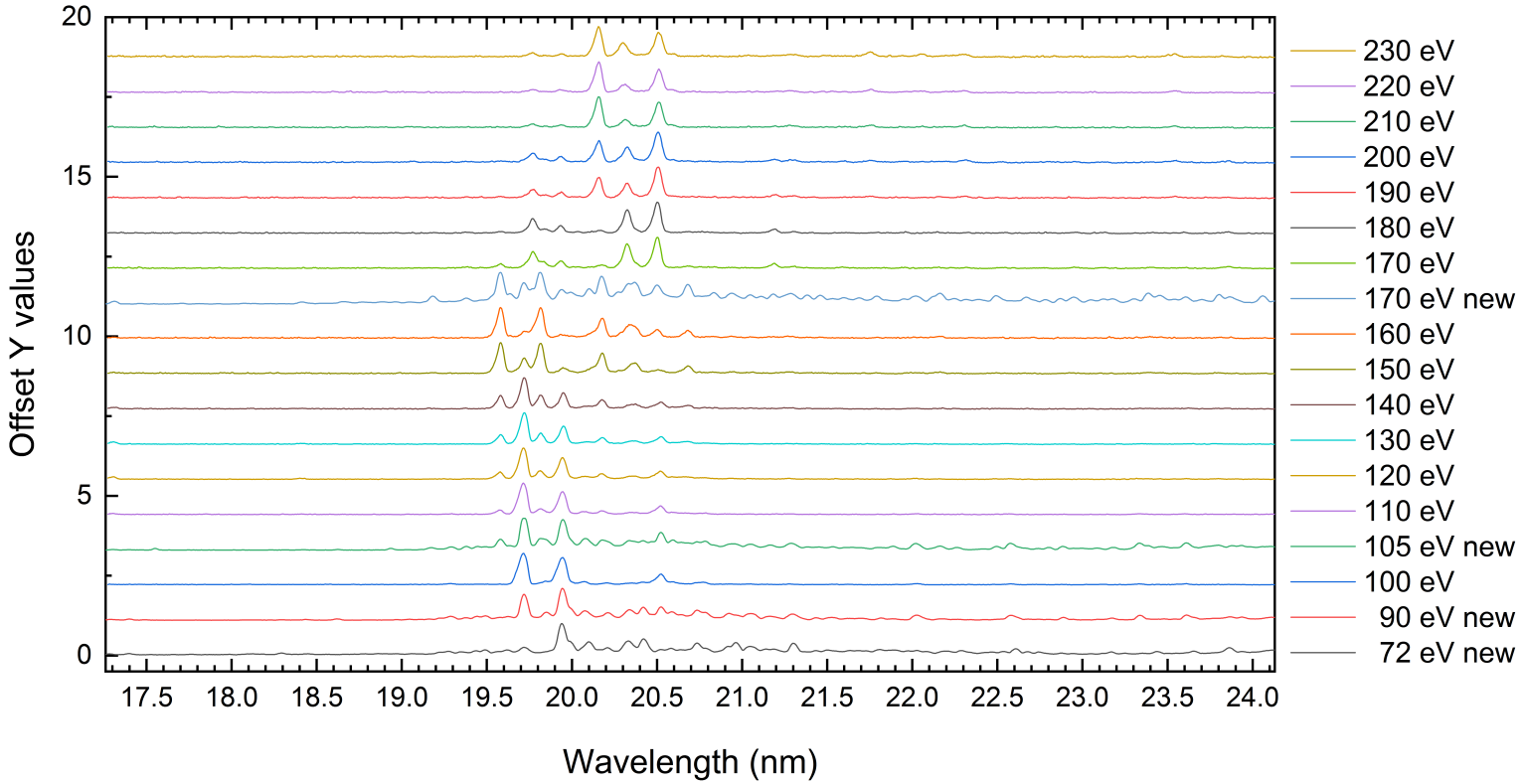

Figure 5.11: Summary plot of the previous [23] and present data. The x-axis was adapted to the wavelength area which is common in both measurements.

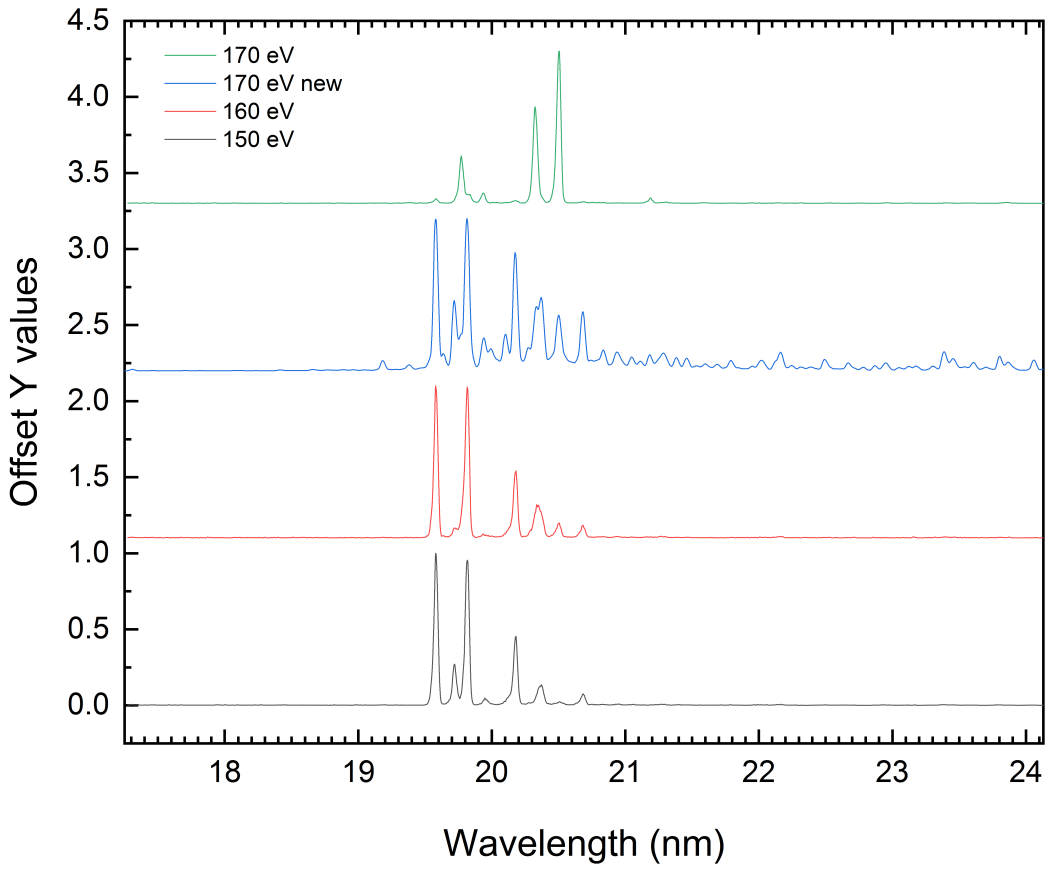

Figure 5.12: Comparision of the present 170 eV measurement with 170 eV, 160 eV and 150 eV.

5.2.4 Charge state identification

By observing the strong peaks appearing, growing, and fading at different electron beam energies, some approximation can be made about the charge states of these lines using the known ionization potentials of ruthenium listed in table 5.12.

If considering those values it could be theoretically possible to observe lines up to a charge state of Ru^{8+}. Nevertheless one has to consider the influence of the space charge which is reducing the effective electron beam energy by a certain amount. One should notice that all the energies mentioned are not space charge corrected.

Again, a comparison between the present and previous data from J. Jäger can be done.

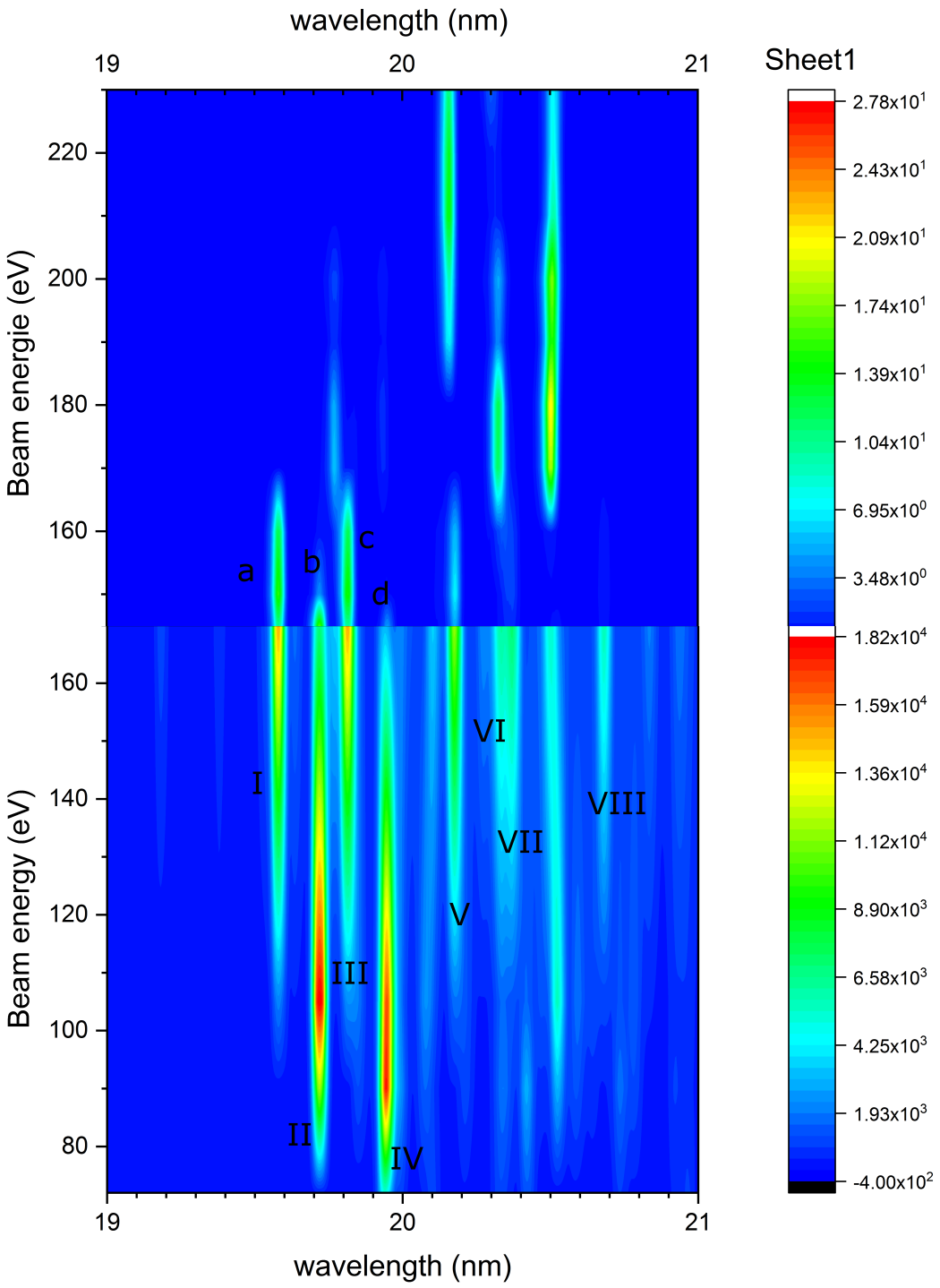

Figure 5.13: 2D plot of previous data [23] (above) and the present (below) data overlaid for illustration purpose. This plot is a rough assumption based on the discussion before were the previous data is overlapping with the present one. Labels a-d are corresponding to the labels in [23] and I-VIII to the labeling in the further analysis.

In Figure 5.13 the development of certain lines as functions of the beam energy is depicted very intuitively. One can easily observe that this measurements were able to extend the data for low charge states of ruthenium ever further. Likewise more information is achieved about the charge state from lines of previous measurements like b and d.

In the following a table of ten strong lines is provided which are common in the measurement at electron beam energy of 170 eV, 105 eV, 90 eV and 72 eV. By analyzing the evolution of theses lines from 170 eV to 72 eV an attempt is made to assign a certain charge state to the lines in consideration of the needed ionization energies and the space charge. To facilitate the observation of the lines developing all four spectra are displayed in Figure 5.14.

Table 5.12: In this tabular again the energies which are necessary to produce the charge states Ru^{3+} to Ru^{8+} are summarized.

Charge state	**Scotfield** [eV]	**NIST** [eV]	**Configuration**
Ru^{3+}	29.4	28.47	$[Kr]4d^6$
Ru^{4+}	43.5	45.0 ± 1.7	$[Kr]4d^5$
Ru^{5+}	58.7	59.0 ± 1.9	$[Kr]4d^4$
Ru^{6+}	74.9	76.0 ± 2.0	$[Kr]4d^3$
Ru^{7+}	92.7	93.0 ± 2.0	$[Kr]4d^2$
Ru^{8+}	110.9	110.0 ± 2.1	$[Kr]4d$
Ru^{9+}	178.5	138.41 ± 0.05	$[Ar]3d^{10}4s^24p^6$

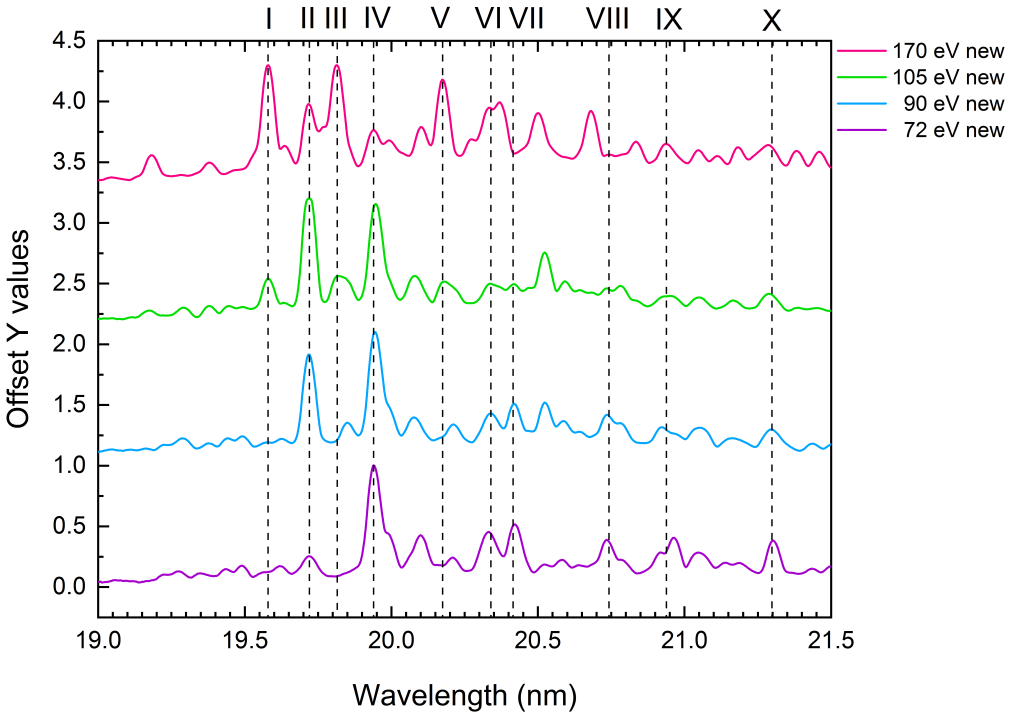

Figure 5.14: The measured spectra at electron beam energy of 170 eV, 105 eV, 90 eV and 72 eV are plotted here with straight vertical lines indicating the examined lines labeled with roman numbers.

Following the reasons for assigning a line to a certain charge state are listed:

- Line I and III:

  These lines are also appearing in previous measurements (see Figure 5.13 line labeled with a and c). They are the two strongest lines in the measurement at 170 eV. Their intensity is decreasing when going down to 105 eV. At lower energies these lines are not observed. Hence it is concluded they must belong to a charge state which is higher populated at 170 eV but also ionized at 105 eV.

  $\Rightarrow$ Ru^{6+} or Ru^{7+} (which is less likely to be present in 105 eV taking into account the space charge).

- Line II:

  Present in the previous measurements (line labeled with c) and in all the measured energies in the new measurement. From beam energy of 170 eV to 72 eV the line is first gaining intensity by making its strongest appearance in 105 eV and then decreasing again. Its charge state must be still present at 72 eV.

  $\Rightarrow Ru^{5+}$

- Line IV:

  Again turning up in J. Jägers measurements (Line labeled with d). Like line II it has a low intensity at 170 eV compared to the strong peaks of line I and III. Contrary to line II its height is increasing when going down to 72 eV representing the strongest peak at 90 eV and 72 eV.

  $\Rightarrow Ru^{4+}$

- Line V:

  Similar behavior as lines I and III, but with slightly lower intensity at 170 eV.

  $\Rightarrow Ru^{6+}$

- Line VI:

  This line seems to be a blend of at least two lines and maybe even different charge states at 170 eV. Its intensity is first decreasing with the electron beam energy and then increasing again from 90 eV to 72 eV. It could be a low charge state which is less populated in the higher energies, overlapping maybe with a high charge state in 170 eV

  $\Rightarrow Ru^{3+}$ and Ru^{7+}

- Line VII and VIII:

  Showing the same behavior as line VI but without an overlapping of a different charge state in the high energy, because it disappears at 170 eV.

  $\Rightarrow Ru^{3+}$

- Line IX and X:

  Behavior is similar to line VI. Blending of two charge state, because the lines are appearing

at 170 eV with higher intensity than at 105 eV and are getting strong again in 90 eV and 72 eV .

$\Rightarrow$ Ru^{3+} and Ru^{7+}

Additionally, it should be mentioned that lower charge states can be excluded because these cannot be observed in the EUV spectrometer energy range. As mentioned in chapter 4 also spectra down to 44 eV were taken with the VUV spectrometer. During these measurements of 55 eV and 40 eV the EUV spectrometer was also taking spectra. Unfortunately, in these spectra, no lines were seen. Hence, low charge states cannot be observed in the EUV range.

Table 5.13: Common strong lines in the open injection of 170 eV, 105 eV, 90 eV and 72 eV and their assumed charge state of ruthenium

Label 5.13	**Ru charge state**	**Label**	170 eV λ [nm]	**Label**	105 eV λ [nm]	**Label**	90 eV λ [nm]	**Label**	72 eV λ[nm]
I	Ru^{6+} Ru^{7+}	12	19.580 (10)	9	19.581 (10)				
II	Ru^{5+}	13	19.722 (11)	10	19.719 (10)	16	19.719 (10)	13	19.720 (10)
III	Ru^{6+} Ru^{7+}	14	19.813 (11)	11	19.828 (11)	17	19.851 (14)		
IV	Ru^{4+}	15	19.943 (14)	12	19.948 (11)	18	19.946 (11)	14	19.942 (11)
V	Ru^{6+}	18	20.176 (12)	14	20.187 (12)	20	20.212 (15)	16	20.206 (17)
VI	Ru^{3+} Ru^{7+}	19	20.356 (12)	15	20.346 (12)	21	20.339 (12)	17	20.333 (12)
V II	Ru^{3+}			16	20.418 (13)	22	20.420 (12)	18	20.421 (12)
V III	Ru^{3+}			19	20.731 (15)	26	20.744 (13)	20	20.737 (13)
IX	Ru^{3+} Ru^{7+}	23	20.940 (14)	21	20.942 (14)	27	20.930 (14)	21	20.961 (14)
X	Ru^{3+} Ru^{7+}	27	21.282 (15)	24	21.289 (15)	30	21.297 (15)	23	21.303 (15)

5.2.5 Comparison with theory

For comparison computational collisional radiative models for Ru^{5+} and Ru^{6+} were run by C. Shah, to get a quick overview of the agreement between experiment and theory. The results are displayed in the Figures 5.15 and 5.16. Here again the *normalize to [1,0] function* of *Origin* was used to compare spectra of different intensities. The lines with high intensity which show up at the long wavelength parts of the CRM spectra are not matching at all with the experimental data. In the middle, there are some lines matching but their intensity is not congruent with the measured one. This is likewise the case in the comparison with the Ru^{6+} CRM spectra although this seems to fit better with the experimental data. The predicted strong lines are slightly off the measured ones. Therefore it is not possible in the context of this thesis to assign certain transitions to the observed lines. It has to been noted that the theoretical treatment of systems with 38 or 39 electrons is quite complex. By varying the terms and conditions of the calculations the results might be improved to find theoretical spectra which match with the observations. However, this work is not the scope of this thesis and it should be investigated further in the future.

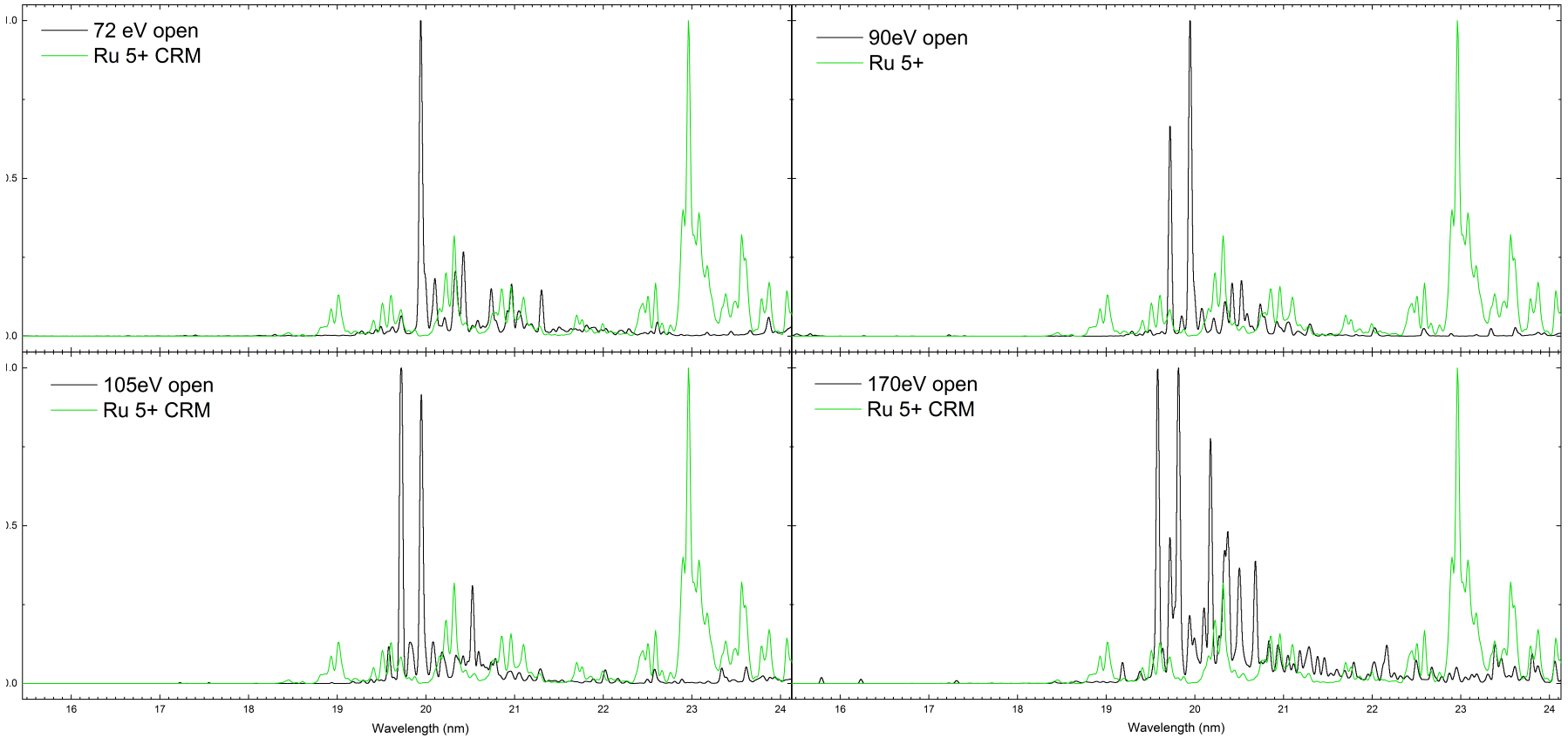

Figure 5.15: The measurements with open injection for 170 eV, 105 eV, 90 eV and 72 eV are overlaid with the calculated the collisional radiative model (CRM) of Ru^{5+}. The intensities of the measured spectra and the simulated CRM are normalized to 1.

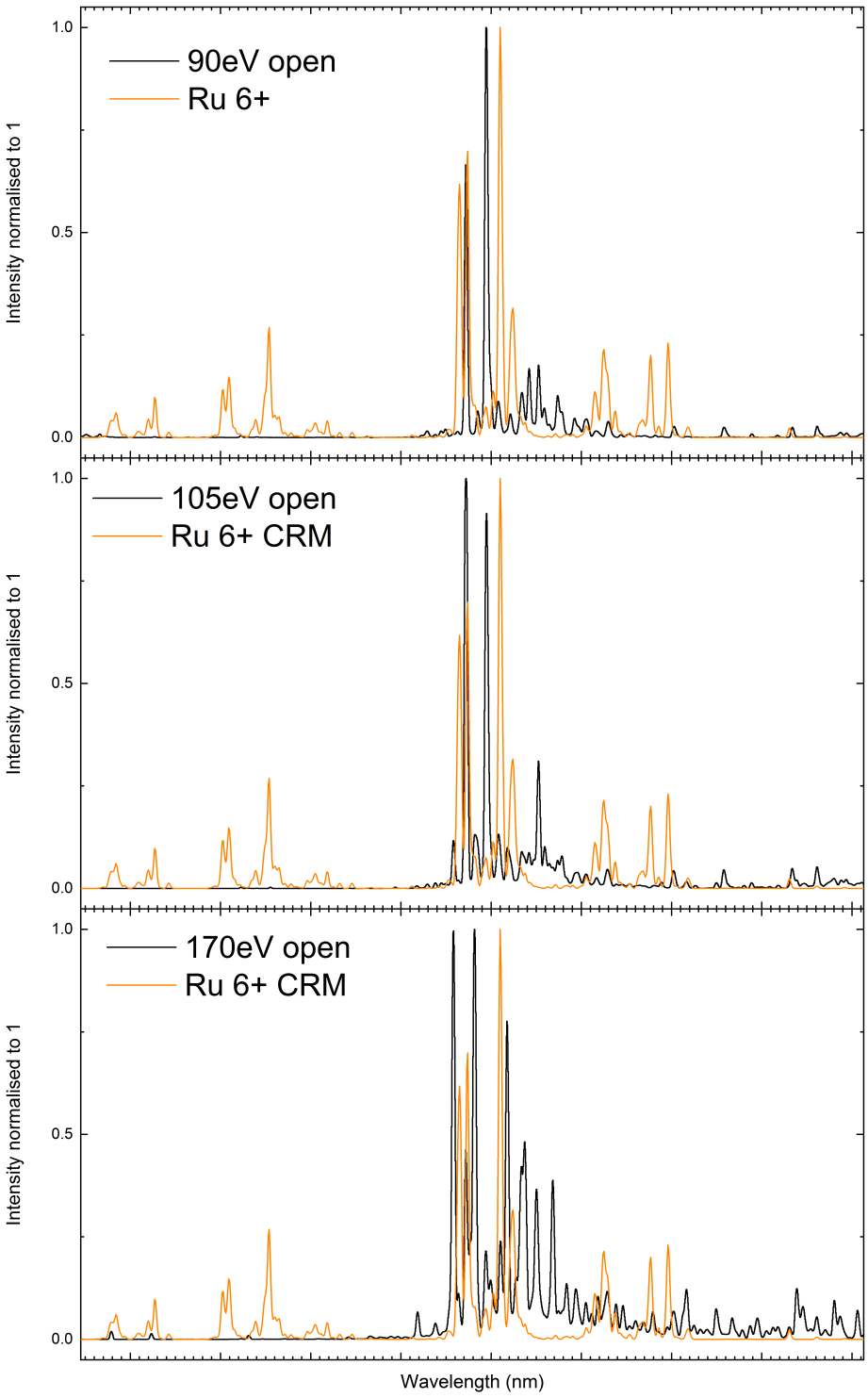

Figure 5.16: The measurements with open injection for 170 eV, 105 eV, 90 eV and 72 eV are overlaid with the calculated the collisional radiative model (CRM) of Ru^{6+}. The intensities of the measured spectra and the simulated CRM are normalized to 1.

Chapter 6

Conclusion

The aim of this thesis was to observe the low charge states of ruthenium from Ru^{+3} to Ru^{+7} with extreme ultraviolet spectroscopy in an electron beam ion trap and identify the elements and charge states of other strong lines observed in the recorded spectra. For this purpose, challenging measurements at low electron beam energies down to 72 eV were performed, which was done for the first time. The atomic data of the measured ruthenium lines extend the available experimental data towards low charge states beyond what was available before. This knowledge might be useful to identify ruthenium and eventually technetium in astronomical observations of stellar objects like white dwarfs. Additionally, the identification of charge states provides a useful benchmark of theory to test complex calculations of many-electron systems.

Ruthenium was injected in the form of an organometallic compound into the trap and measurements with open and closed injection system at uncorrected electron beam energies of 170 eV, 105 eV, 90 eV and 72 eV were performed. The spectra were recorded with the EUV spectrometer within a wavelength range from 15 nm to 24 nm. The electron beam current was reduced during the measurements to maintain a constant electron beam density N_e. The trap settings were also adjusted for the different electron beam energies. This was crucial at low electron beam energies to achieve the maximum number of electrons reaching the trap and not being deflected due to too low velocities. The resulting spectra were corrected for their line shifts,

cosmics and underground before analysis. For calibration the spectra recorded with a closed injection system and showing strong oxygen lines of the charge states O VI, O V and O IV were used. The line positions were fitted with a polynomial function which was applied to the spectra to convert the instrumental scale from pixel into wavelength. The results of this calibration agree with data from previous measurements [23]. Nevertheless, this calibration might be improved by not only analyzing the spectra recorded with closed injection but performing a calibration measurement with a well-known spectrum of an element like iron before the actual measurements. However, then problems with iron lines contaminating spectra taken afterwards might occur since iron is difficult to remove from the trap. An analysis of the spectra measured for this thesis led to the conclusion that the most prominent impurities are from oxygen and nitrogen and have no relevant impact on the quality of the acquired spectra.

Finally, the strong lines in the spectra were analyzed for ruthenium. Firstly, a comparison with previous measurements showed the agreement of all strong lines. The present measurement could be improved in comparison to the previous one, resulting in higher intensities and more lines observed at low beam energies. The appearance and disappearance of different charge states with changing electron beam energies (230 eV to72 eV; see Figure 5.11) could be observed. Subsequent to this the strong lines of the present spectra were analyzed for the charge states of ruthenium. This analysis could be potentially extended by applying corrections for the negative space charge caused by the electron beam and the positive space charge caused by the ions. Currently, those corrections are only estimations and not expected to be linear for low electron beam energies. A more sophisticated analysis should be carried out to confirm the identification of certain charge states.

In addition, the spectra were compared with a computational collisional radiative model for the charge states Ru^{5+} and Ru^{6+}. Unfortunately, those were not in agreement with the experimental data especially for the lines with high intensities. Consequently, the lines identified with a charge state before could not be assigned to certain transitions. However, this disagreement is not unusual. The computation requires complex calculations for systems with many electrons (Ru, $Z = 44$) where not all processes are fully understood. In future analyses, additional

calculations with the Flexible Atomic Code (FAC) might have to be performed to identify computational parameters better reproducing the experimental data [25]. The detailed analysis carried out in this thesis should facilitate the line identification once a matching theoretical approach is found.

In conclusion, the measurements performed during this thesis provide data for low charge states of ruthenium which were not available before. In addition, the spectra recorded with the VUV spectrometer simultaneous with the measurements discussed in this thesis provide data for even lower charge states and a different wavelength region. In continuation similar measurements for technetium should be performed, for which the executed measurements provide a good orientation. This will require an adaption of the injection system due to the radioactive nature of this element. All this might help to prove the presence of technetium in the white dwarf *RE 0503-289* [5].

Appendix

The lines of impurity elements identified in the open injections of the measurements at electron beam energies of 170 eV, 105 eV, 90 eV and 72 eV, are listed here (see section 5.2.2).

Table 1: 170 eV identified lines impurity lines in open injection

Label	**Charge state**	**Configuration**	λ_{Exp} [nm]	λ_{Obs} [nm]	**Int.**	λ_{Ritz} [nm]	**Transition rate** [s^{-1}]	$\Delta_{Exp-Obs}$ [nm]	$\Delta_{Ritz-Obs}$ [nm]
1	N V	$1s^2 2p(3/2) - 1s^2 6d(5/2)$	15.787 (3)	15.8088 (3)	360	15.8088 (10)	3.62E+09	0.022	0.022
2	N V	$1s^2 2s(1/2) - 1s^2 4p(3/2)$	16.232 (4)	16.2556 (3)	480	16.2556 (10)	5.79E+09	0.024	0.024
3	O VI	$1s^2 2p(3/2) - 1s^2 3s(1/2)$	17.310 (5)	17.3082 (50)	1000	17.3079 (10)	1.46E+10	0.002	0.002
4	O VI	$1s^2 2p(3/2) - 1s^2 3d(5/2)$	18.416 (8)	18.4117 (175)	850	18.4117 (10)	1.14E+10	0.005	0.005
7	N IV	$1s^2 2s2p(2) - 1s^2 2s8d(3)$	18.887 (9)	18.8818 (2)	300	18.8818 (10)	2.23E+08	0.006	0.006
8	N IV	$1s^2 2s2p(2) - 1s^2 2p(2P^\circ 3/2)4p(1)$	18.963 (9)	18.9437 (3)	10	18.9437 (10)	9.99E+08	0.019	0.019
9	N V	$1s^2 2p(3/2) - 1s^2 4s(1/2)$	19.050 (9)	19.0249 (2)	320	19.0249 (10)	2.30E+09	0.025	0.025
10	N IV	$1s^2 2s2p(2) - 1s^2 2p(2P^\circ)4p(2)$	19.183 (9)	19.1700 (1000)	400	19.1702 (10)	1.95E+09	0.013	0.013
12	O IV	$2s^2 2p(3/2) - 2s^2 4d(5/2)$	19.580 (10)	19.6010 (100)	200	19.6006 (10)	1.20E+10	0.021	0.021
13	N IV	$1s^2 2s^2(0) - 1s^2 2s4p(1)$	19.722 (11)	19.7230 (100)	500	19.7228 (10)	6.01E+09	0.001	0.001
15	N IV	$1s^2 2p2(2) - 1s^2 2p(2P^\circ)8d(2)$	19.943 (14)			19.9159 (10)	3.63E+08		0.027
	N IV	$1s^2 2p2(2) - 1s^2 2p(2P^\circ)8d(3)$		19.9159 (2)	450			0.027	0.000
17	O IV	$2s^2 p2(5/2) - 2s2p(3P^\circ)4s(5/2)$	20.101 (13)	20.0995 (3)	5	20.0994 (10)	2.57E+09	0.001	0.001
20	O V	$1s^2 2p^2(2) - 1s^2 2p(2P^\circ{}_{3/2})3d(1)$	20.501 (12)	20.5105 (2)	150	20.5106 (10)	2.26E+09	0.010	0.010
21	O IV	$2s^2 2p(1/2) - 2s2p(3P^\circ)3p^(3/2)$	20.681 (13)	20.7180 (100)	110	20.7183 (10)	1.18E+10	0.037	0.037

22	N IV	$1s^2 2p^2(2) - 1s^2 2p(2P^\circ)6d(3)$	20.832 (14)	20.8150 (3)	400	20.8150 (10)	3.57E+09	0.017	0.017
23	N V	$1s^2 2s(1/2) - 1s^2 3p(1/2)$	20.940 (14)	20.9303 (10)	90	20.9308 (10)	1.21E+10	0.010	0.009
26	N IV	$1s^2 2s2p(1) - 1s^2 2s9d(2)$	21.188 (14)	21.1679 (2)	250	21.1679 (10)	5.01E+08	0.020	0.020
27	O IV	$2s^2 p2(5/2) - 2s2p(3P^\circ)4d(7/2)$	21.282 (15)	21.2974 (3)	10	21.2975 (10)	1.05E+10	0.016	0.016
30	O V	$1s^2 2p^2(2) - 1s^2 2p(2P^\circ{}_{1/2})3d(2)$	21.595 (16)	21.6018 (10)	250	21.6019 (10)	3.07E+10	0.007	0.007
31	N IV	$1s^2 2s2p(1) - 1s^2 2p(2P^\circ 3/2)4p(2)$	21.686 (17)	21.7200 (100)	500	21.7218 (10)	3.70E+09	0.034	0.036
32	N IV	$2p^2(2) - 2p5d(2)$	21.792 (16)	21.7900 (100)	500			0.002	
34	O V	$1s^2 2s2p(1) - 1s^2 2s3d(2)$	22.022 (17)	22.0352 (10)	520	22.0353 (10)	4.29E+10	0.014	0.014
35	O IV	$2s^2 p^2(1/2) - 2p^2(3P)3p(3/2)$	22.159 (17)	22.1648 (3)	15			0.006	
	O IV	$2s^2 p2(3/2) - 2p^2(1D)3p(3/2)$				22.1637 (10)	7.20E+08	0.000	0.005
39	N IV	$1s^2 2s2p(0) - 1s^2 2s4d(1)$	22.496 (18)	22.5120 (100)	800	22.5108 (10)	5.57E+09	0.016	0.014
41	O V	$1s^2 2p^2(2) - 1s^2 2p(2P^\circ{}_{1/2})3s(1)$	22.780 (20)	22.7689 (10)	80	22.7689 (10)	5.72E+09	0.011	0.011
45	O IV	$2s^2 p2(5/2) - 2s2p(3P^\circ)3d(3/2)$	23.122 (21)	23.1239 (2)	40	23.1239 (10)	1.29E+10	0.002	0.002
46	O V	$1s^2 2p^2(0) - 1s^2 2p(2P^\circ{}_{3/2})3d(1)$	23.178 (21)	23.1823 (10)	150	23.1822 (10)	4.36E+10	0.004	0.004
47	O IV	$2s2p^2(1/2) - 2s2p(3P^\circ)3d(3/2)$	23.302 (21)	23.3457 (3)	60	23.3451 (10)	2.20E+10	0.044	0.043
49	N IV	$1s^2 2s2p(2) - 1s^2 2p(2P^\circ)3p(1)$	23.456 (21)	23.4250 (100)	600	23.4251 (10)	1.98E+09	0.031	0.031
51	N IV	$1s^2 2s2p(1) - 1s^2 2s5d(2)$	23.606 (22)	23.6070 (100)	550	23.6068 (10)	3.35E+09	0.001	0.000
53	N IV	$1s^2 2s2p(2) - 1s^2 2s4s(1)$	23.804 (23)	23.7990 (100)	500	23.7987 (10)	4.84E+09	0.005	0.006
54	N IV	$1s^2 2p^2(1) - 1s^2 2p(2P^\circ)4d(1)$	23.872 (23)	23.8700 (1000)	500	23.8698 (10)	1.31E+09	0.002	0.002

Table 2: 105 eV identified lines impurity lines in open injection

Label	**Charge state**	**Configuration**	λ_{Exp} [nm]	λ_{Obs} [nm]	**Int.**	λ_{Ritz} [nm]	**Transition rate** [s^{-1}]	$\Delta_{Exp-Obs}$ [nm]	$\Delta_{Ritz-Obs}$ [nm]
1	O V	$1s^2 2s^2(0) - 1s^2 2s3p(1)$	17.225 (5)	17.2169 (10)	450	17.2169 (10)	2.94E+10	0.008	0.008
4	N V	$1s^2 2p(3/2) - 1s^2 4d(5/2)$	18.627 (8)	18.6153 (10)	62	18.6149 (10)	1.42E+10	0.011	0.012
5	N IV	$1s^2 2s2p(0) - 1s^2 2p(2P^\circ_{3/2})4p(1)$	18.936 (9)	18.9365 (2)	1	18.9363 (10)	2.00E+08	0.000	0.000
6	N IV	$1s^2 2s2p(2) - 1s^2 2p(2P^\circ)4p(2)$	19.175 (9)	19.1700 (1000)	400	19.1702 (10)	1.95E+09	0.005	0.005
7	O V	$1s^2 2s2p(2) - 1s^2 2s3d(3)$	19.291 (9)	19.2906 (10)	520	19.2904 (10)	6.89E+10	0.000	0.000
9	O IV	$2s^2 2p(3/2) - 2s^2 4d(5/2)$	19.581 (10)	19.6010 (100)	200	19.6006 (10)	1.20E+10	0.020	0.020
10	N IV	$1s^2 2s^2(0) - 1s^2 2s4p(1)$	19.719 (10)	19.7230 (100)	500	19.7228 (10)	6.01E+09	0.004	0.004
11	O IV	$2s^2 p2(3/2) - 2p^2(1D)3p(3/2)$	19.828 (11)			19.8034 (10)	5.90E+09		0.024
12	N IV	$1s^2 2p2(2) - 1s^2 2p(2P^\circ)8d(2)$	19.948 (11)			19.9159 (10)	3.63E+08		0.032
13	O IV	$2s^2 p2(5/2) - 2s2p(3P^\circ)4s(5/2)$	20.081 (12)	20.0995 (3)	5	20.0994 (10)	2.57E+09	0.019	0.018
15	O IV	$2s^2 2p(3/2) - 2s2p(3P^\circ)3p(1/2)$	20.346 (45)	20.3044 (2)	25	20.3044 (10)	7.05E+09	0.041	0.041
16	O V	$1s^2 2p^2(2) - 1s^2 2p(2P^\circ_{3/2})3d(3)$	20.418 (13)	20.3890 (100)	200	20.3890 (10)	8.16E+10	0.029	0.029
17	O V	$1s^2 2p^2(2) - 1s^2 2p(2P^\circ_{3/2})3d(1)$	20.523 (13)	20.5105 (2)	150	20.5106 (10)	2.26E+09	0.013	0.013
18	N IV	$1s^2 2s^2(0) - 1s^2 2s5d(1)$	20.596 (13)	20.5940 (100)	500	20.5939 (10)	2.77E+09	0.002	0.002
19	O IV	$2s^2 2p(3/2) - 2s2p(3P^\circ)3p(5/2)$	20.731 (15)	20.7240 (100)	150	20.7239 (10)	1.18E+10	0.007	0.007

20	O V	$1s^2 2p^2(2) - 1s^2 2p(2P^\circ_{3/2})3d(3)$	20.780 (14)	20.7794 (10)	300	20.7796 (10)	8.58E+10	0.001	0.000
21	N V	$1s^2 2s(1/2) - 1s^2 3p(1/2)$	20.942 (14)	20.9303 (10)	90	20.9308 (10)	1.21E+10	0.012	0.011
23	N IV	$1s^2 2s2p(1) - 1s^2 2s9d(2)$	21.166 (14)	21.1679 (2)	250	21.1679 (10)	5.01E+08	0.002	0.002
24	O IV	$2s^2 p2(5/2) - 2s2p(3P^\circ)4d(7/2)$	21.289 (15)	21.2974 (3)	10	21.2975 (10)	1.05E+10	0.008	0.008
27	O V	$1s^2 2s2p(2) - 1s^2 2s3s(1)$	21.532 (15)	21.5245 (10)	250	21.5245 (10)	1.02E+10	0.007	0.007
28	O V	$1s^2 2p^2(2) - 1s^2 2p(2P^\circ 1/2)3d(2)$	21.638 (16)	21.6018 (10)	250	21.6019 (10)	3.07E+10	0.036	0.036
29	N IV	$2p^2(2) - 2p5d(2)$	21.807 (17)	21.7900 (100)	500			0.017	
31	O V	$1s^2 2s2p(1) - 1s^2 2s3d(2)$	22.022 (17)	22.0352 (10)	520	22.0353 (10)	4.29E+10	0.013	0.013
32	O IV	$2s^2 p^2(1/2) - 2p^2(3P)3p(3/2)$	22.162 (17)	22.1648 (3)	15			0.003	
	O IV	$2s^2 p2(3/2) - 2p^2(1D)3p(3/2)$				22.1637 (10)	7.20E+08	0.000	0.002
34	N IV	$1s^2 2s2p(0) - 1s^2 2s4d(1)$	22.496 (18)	22.5120 (100)	800	22.5108 (10)	5.57E+09	0.016	0.015
38	O V	$1s^2 2p^2(0) - 1s^2 2p(2P^\circ_{3/2})3d(1)$	23.182 (21)	23.1823 (10)	150	23.1822 (10)	4.36E+10	0.001	0.001
39	O IV	$2s^2 p^2(1/2) - 2s2p(3P^0)3d(1/2)$	23.338 (21)	23.3460 (100)	140	23.3466 (10)	4.40E+10	0.008	0.008
40	N IV	$1s^2 2s2p(1) - 1s^2 2s5d(2)$	23.612 (22)	23.6070 (100)	550	23.6068 (10)	3.35E+09	0.005	0.005
41	N IV	$1s^2 2s2p(2) - 1s^2 2s4s(1)$	23.793 (23)	23.7990 (100)	500	23.7987 (10)	4.84E+09	0.006	0.006
42	N IV	$1s^2 2p^2(1) - 1s^2 2p(2P^\circ)4d(1)$	23.880 (23)	23.8700 (1000)	500	23.8698 (10)	1.31E+09	0.010	0.010
43	N IV	$1s^2 2s2p(1) - 1s^2 2p(2P^\circ)3p(2)$	23.934 (23)	23.9620 (100)	500	23.9619 (10)	3.19E+09	0.028	0.028

Table 3: 90 eV identified lines impurity lines in open injection

Label	**Charge state**	**Configuration**	λ_{Exp} [nm]	λ_{Obs} [nm]	**Int.**	λ_{Ritz} [nm]	**Transition rate** [s^{-1}]	$\Delta_{Exp-Obs}$ [nm]	$\Delta_{Ritz-Obs}$ [nm]
3	N V	$1s^2 2s(1/2) - 1s^2 4p(3/2)$	16.266 (4)	16.2556 (3)	480	16.2556 (10)	5.79E+09	0.011	0.011
4	N V	$1s^2 2p(1/2) - 1s^2 5d(3/2)$	16.637 (4)	16.6875 (2)	440	16.6875 (10)	5.48E+09	0.051	0.051
5	O V	$1s^2 2s^2(0) - 1s^2 2s3p(1)$	17.225 (5)	17.2169 (10)	450	17.2169 (10)	2.94E+10	0.008	0.008
7	O IV	$2s^2 2p(3/2) - 2s2p(3P^\circ)4p(1/2)$	17.400 (5)	17.3968 (2)	1	17.3969 (10)	1.52E+09	0.003	0.003
9	N V	$1s^2 2p(3/2) - 1s^2 4d(5/2)$	18.622 (8)	18.6153 (10)	62	18.6149 (10)	1.42E+10	0.006	0.007
10	O IV	$2s^2 p^2(5/2) - 2s2p(3P^\circ)4d(5/2)$	19.233 (9)	19.2244 (3)	10	19.2231 (10)	6.59E+09	0.009	0.010
11	O V	$1s^2 2s2p(2) - 1s^2 2s3d(3)$	19.289 (9)	19.2906 (10)	520	19.2904 (10)	6.89E+10	0.002	0.002
13	O V	$1s^2 2s2p(1) - 1s^2 2p(2P^\circ{}_{1/2})3p(1)$	19.442 (10)	19.4593 (10)	200	19.4592 (10)	1.73E+10	0.017	0.017
15	O IV	$2s^2 2p(3/2) - 2s^2 4d(5/2)$	19.625 (10)	19.6010 (100)	200	19.6006 (10)	1.20E+10	0.024	0.024
16	N IV	$1s^2 2s^2(0) - 1s^2 2s4p(1)$	19.719 (10)	19.7230 (100)	500	19.7228 (10)	6.01E+09	0.004	0.003
17	O IV	$2s^2 p2(3/2) - 2p^2(1D)3p(3/2)$	19.852 (14)			19.8034 (10)			0.048
19	O IV	$2s^2 p2(5/2) - 2s2p(3P^\circ)4s(5/2)$	20.078 (12)	20.0995 (3)	5	20.0994 (10)	2.57E+09	0.021	0.021
21	O IV	$2s^2 2p(3/2) - 2s2p(3P^\circ)3p(1/2)$	20.339 (12)	20.3044 (2)	25	20.3044 (10)	7.05E+09	0.034	0.034
22	O V	$1s^2 2p^2(2) - 1s^2 2p(2P^\circ{}_{3/2})3d(3)$	20.420 (12)	20.3890 (100)	200	20.3890 (10)	8.16E+10	0.031	0.031
23	O V	$1s^2 2p^2(2) - 1s^2 2p(2P^\circ{}_{3/2})3d(1)$	20.524 (13)	20.5105 (2)	150	20.5106 (10)	2.26E+09	0.014	0.014
24	N IV	$1s^2 2s^2(0) - 1s^2 2s5d(1)$	20.592 (13)	20.5940 (100)	500	20.5939 (10)	2.77E+09	0.002	0.002

26	O IV	$2s^2 2p(3/2) - 2s2p(3P^\circ)3p(5/2)$	20.744 (13)	20.7240 (100)	150	20.7239 (10)	1.18E+10	0.020	0.020
27	N V	$1s^2 2s(1/2) - 1s^2 3p(1/2)$	20.930 (14)	20.9303 (10)	90	20.9308 (10)	1.21E+10	0.000	0.001
29	N IV	$1s^2 2s2p(1) - 1s^2 2s9d(2)$	21.167 (18)	21.1679 (2)	250	21.1679 (10)	5.01E+08	0.001	0.001
30	O IV	$2s^2 p2(5/2) - 2s2p(3P^\circ)4d(7/2)$	21.297 (15)	21.2974 (3)	10	21.2975 (10)	1.05E+10	0.000	0.000
31	O IV	$2s^2 p2(3/2) - 2s2p(3P^\circ)4d(3/2)$	21.437 (15)	21.4290 (3)	2	21.4281 (10)	2.41E+09	0.008	0.009
32	O V	$1s^2 2s2p(2) - 1s^2 2s3s(1)$	21.527 (15)	21.5245 (10)	250	21.5245 (10)	1.02E+10	0.002	0.002
33	O V	$1s^2 2p^2(2) - 1s^2 2p(2P^\circ 1/2)3d(2)$	21.626 (16)	21.6018 (10)	250	21.6019 (10)	3.07E+10	0.025	0.024
34	N IV	$1s^2 2s2p(1) - 1s^2 2p(2P^\circ 3/2)4p(2)$	21.701 (16)	21.7200 (100)	500	21.7218 (10)	3.70E+09	0.019	0.021
35	N IV	$2p^2(2) - 2p5d(2)$	21.818 (16)	21.7900 (100)	500			0.028	
37	O V	$1s^2 2s2p(1) - 1s^2 2s3d(2)$	22.028 (17)	22.0352 (10)	520	22.0353 (10)	4.29E+10	0.007	0.007
38	O IV	$2s^2 p^2(1/2) - 2p^2(3P)3p(3/2)$	22.175 (21)	22.1648 (3)	15			0.010	
	O IV	$2s^2 p2(3/2) - 2p^2(1D)3p(3/2)$				22.1637 (10)			0.011
41	O V	$1s^2 2p^2(0) - 1s^2 2p(2P^\circ_{3/2})3d(1)$	23.172 (21)	23.1823 (10)	150	23.1822 (10)	4.36E+10	0.010	0.010
42	O IV	$2s^2 p^2(1/2) - 2s2p(3P^0)3d(1/2)$	23.339 (21)	23.3460 (100)	140	23.3466 (10)	4.40E+10	0.007	0.007
43	N IV	$1s^2 2s2p(1) - 1s^2 2s5d(2)$	23.616 22 (22)	23.607 (100)	550	23.6068 (10)	3.35E+09	0.009	0.009
44	N IV	$1s^2 2s2p(2) - 1s^2 2s4s(1)$	23.794 88 (23)	23.799 (100)	500	23.7987 (10)	4.84E+09	0.004	0.004
45	O IV	$2s^2 2p(3/2) - 2s^2 3d(5/2)$	23.867 28 (23)	23.857 (100)	180	23.857 (10)	3.54E+10	0.010	0.010
46	N IV	$1s^2 2s2p(1) - 1s^2 2p(2P^\circ)3p(2)$	23.938 06 (23)	23.962 (100)	500	23.9619 (10)	3.19E+09	0.024	0.024

Table 4: 72 eV identified lines impurity lines in open injection

Label	**Charge state**	**Configuration**	λ_{Exp} [nm]	λ_{Obs} [nm]	**Int.**	λ_{Ritz} [nm]	**Transition rate** [s^{-1}]	$\Delta_{Exp-Obs}$ [nm]	$\Delta_{Ritz-Obs}$ [nm]
1	O IV	$2s^2 2p(3/2) - 2s2p(3P^\circ)4p(1/2)$	17.397 (7)	17.3968 (2)	1	17.3969 (10)	1.52E+09	0.001	0.001
2	O IV	$2s^2 2p(1/2) - 2s^2 5d(3/2)$	18.118 (8)	18.1150 (3)	15	18.1150 (10)	5.00E+09	0.003	0.003
3	O IV	$2s^2 2p(3/2) - 2s2p(1P^\circ)3p(5/2)$	18.295 (7)	18.2832 (3)	15	18.2826 (10)	2.09E+09	0.012	0.013
5	N IV	$1s^2 2s2p(2) - 1s^2 2s8s(1)$	18.869 (9)	18.8656 (2)	250	18.8656 (10)	5.03E+07	0.004	0.004
6	N IV	$1s^2 2s2p(2) - 1s^2 2p(2P^\circ{}_{3/2})4p(1)$	18.959 (9)	18.9437 (2)	10	18.9437 (10)	9.99E+08	0.015	0.015
8	N IV	$1s^2 2s2p(2) - 1s^2 2p(2P^\circ)4p(2)$	19.269 (10)	19.1700 (1000)	400	19.1702 (10)	1.95E+09	0.099	0.099
11	N IV	$1s^2 2p^2(0) - 1s^2 2p(2P^\circ)10d(1)$	19.490 (10)			19.5183 (10)	4.06E+08		0.029
12	O IV	$2s^2 2p(3/2) - 2s^2 4d(5/2)$	19.617 (10)	19.6010 (100)	200	19.6006 (10)	1.20E+10	0.016	0.017
13	N IV	$1s^2 2s^2(0) - 1s^2 2s4p(1)$	19.720 (10)	19.7230 (100)	500	19.7228 (10)	6.01E+09	0.003	0.003
15	O IV	$2s^2 p2(5/2) - 2s2p(3P^\circ)4s(5/2)$	20.099 (12)	20.0995 (3)	5	20.0994 (10)	2.57E+09	0.001	0.000
17	O IV	$2s^2 2p(3/2) - 2s2p(3P^\circ)3p(1/2)$	20.333 (12)	20.3044 (2)	25	20.3044 (10)	7.05E+09	0.028	0.028
18	O V	$1s^2 2p^2(2) - 1s^2 2p(2P^\circ{}_{3/2})3d(3)$	20.421 (12)	20.3890 (100)	200	20.3890 (10)	8.16E+10	0.032	0.032
19	N IV	$1s^2 2s^2(0) - 1s^2 2s5d(1)$	20.581 (22)	20.5940 (100)	500	20.5939 (10)	2.77E+09	0.013	0.013
20	O IV	$2s^2 2p(3/2) - 2s2p(3P^\circ)3p(5/2)$	20.737 (13)	20.7240 (100)	150	20.7239 (10)	1.18E+10	0.013	0.013
21	N V	$1s^2 2s(1/2) - 1s^2 3p(1/2)$	20.961 (14)	20.9303 (10)	90	20.9308 (10)	1.21E+10	0.031	0.030
23	O IV	$2s^2 p2(5/2) - 2s2p(3P^\circ)4d(7/2)$	21.303 (15)	21.2974 (3)	10	21.2975 (10)	1.05E+10	0.005	0.005

24	O IV	$2s^2p2(3/2) - 2s2p(3P^\circ)4d(3/2)$	21.433 (16)	21.4290 (3)	2	21.4281 (10)	2.41E+09	0.004	0.004
27	N IV	$1s^22s2p(1) - 1s^22p(2P^\circ 3/2)4p(2)$	21.705 (16)	21.7200 (100)	500	21.7218 (10)	3.70E+09	0.015	0.017
28	N IV	$2p^2(2) - 2p5d(2)$	21.811 (16)	21.7900 (100)	500			0.021	
31	N IV	$1s^22s2p(1) - 1s^22p(2P^\circ 1/2)4p(1)$	22.036 (18)	22.0280 (2)	400	22.0280 (10)	3.03E+09	0.008	0.008
32	O IV	$2s^2p^2(1/2) - 2p^2(3P)3p(3/2)$	22.198 (17)	22.1648 (3)	15			0.034	
	O IV	$2s^2p2(3/2) - 2p^2(1D)3p(3/2)$				22.1637 (10)	7.20E+08		0.035
33	O IV	$2s^2p^2(5/2) - 2s2p(1P^0)3d(5/2)$	22.289 (18)	22.2763 (3)	25	22.2758 (10)	7.66E+09	0.013	0.013
34	N IV	$1s^22s2p(1) - 1s^22s6d(2)$	22.465 (19)	22.4629 (2)	450	22.4629 (10)	1.98E+09	0.002	0.002
35	N IV	$1s^22s2p(2) - 1s^22s4d(3)$	22.536 (19)	22.5210 (100)	800	22.5209 (10)	1.00E+10	0.015	0.015
40	N IV	$1s^22s2p(2) - 1s^22p(2P^\circ)3p(1)$	23.439 (21)	23.4250 (100)	600	23.4251 (10)	1.98E+09	0.014	0.014
41	N IV	$1s^22s2p(1) - 1s^22s5d(2)$	23.654 (22)	23.6070 (100)	550	23.6068 (10)	3.35E+09	0.047	0.047
42	O IV	$2s^22p(3/2) - 2s^23d(5/2)$	23.863 (23)	23.8570 (100)	180	23.8570 (10)	3.54E+10	0.006	0.006
43	N IV	$1s^22s2p(1) - 1s^22p(2P^\circ)3p(2)$	23.943 (23)	23.9620 (100)	500	23.9619 (10)	3.19E+09	0.019	0.019

Bibliography

[1] *Elberfelder Bibel*. Witten: Brockhaus, new american standard version ed., 2006.

[2] W. Demtröder, *Experimentalphysik 4*. SpringerLink : Bücher, Berlin, Heidelberg: Springer Spektrum, 5. aufl. 2017 ed., 2017.

[3] K.-H. Spatschek, *Astrophysik*. SpringerLink : Bücher, Berlin, Heidelberg: Springer Spektrum, 2. aufl. 2018 ed., 2018.

[4] S. Paul und W. Merrill, "Spectroscopic Observations of Stars of Class S," *The Astrophysical Journal*, vol. 116, p. 21, jul 1952.

[5] K. Werner and T. Rauch and S. Kučas and J. W. Kruk, "The prospective search for highly ionized technetium in hot (pre-) white dwarfs," *Astronomy & Astrophysics*, vol. 574, p. A29, jan 2015.

[6] K. W. und J.R. Crespo López-Urrutia, "Search for technetium in extremly hot evolved stars,"

[7] "Nist atomic spectra database lines data." `https://physics.nist.gov/PhysRefData/ASD/lines_form.html`. Accessed: 2018-07-10.

[8] W. Demtröder, *Experimentalphysik 3*. Springer, 4. ed., 2010.

[9] Hermann Haken und Hans Christoph Wolf, *Atom- und Quantenphysik*. Springer, 8. ed., 2004.

[10] L. Täubert, "Extreme ultraviolet spectroscopy of highly charged ruthenium ions," 2017.

[11] S. Epp, *Röntgen–Laserspektroskopie hochgeladener Ionen in einer EBIT am Freie–Elektronen–Laser FLASH.* PhD thesis, Ruprecht-Karls-Universität Heidelberg, 2007.

[12] C. Shah, *Measuring and modeling of anisotropic and polarized x-ray emission following resonant recombination into highly charged ions.* PhD thesis, Ruprecht-Karls-Universität Heidelberg, 2015.

[13] S. Dobrodey, "Untersuchung von K-LL-Resonanzen dielektronischer Rekombination und simultaner Innerschalen-Vakuum-Ultraviolet Übergänge in hochgeladenem Eisen mit einer ElektronenstrahlIonenfalle," Master's thesis, Ruprecht-Karls-Universität Heidelberg, 2014.

[14] L. Brillouin, "A Theorem of Larmor and Its Importance for Electrons in Magnetic Fields," *Phys. Rev.*, vol. 67, pp. 260–266, Apr 1945.

[15] G. Herrmann, "Optical Theory of Thermal Velocity Effects in Cylindrical Electron Beams," *Journal of Applied Physics*, vol. 29, no. 2, pp. 127–136, 1958.

[16] J. Gillaspy, *Trapping Highly Charged Ions: Fundamentals and Applications.* Huntington, New York: Nove Science Publishers, 1999.

[17] S. Bernitt, *Resonante Anregung astrophysikalischer Röntgen-Übergänge in hochgeladenen Eisenionen mit dem Freie-Elektronen-Laser LCLS.* PhD thesis, Ruprecht-Karls-Universität Heidelberg, 2013.

[18] R. S. Orts, *Isotopic effect in B-like and Be-like argon ions.* PhD thesis, Johann-Wolfgang-Goethe Universität Frankfurt, 2005.

[19] T. Baumann, *Spektroskopische Untersuchungen resonanter Rekombinationsprozesse an hochgeladenem Silizium in einer Elektronenstrahl-Ionenfalle.* PhD thesis, Ruprecht-Karls-Universität Heidelberg, 2012.

[20] T. Baumann, "Entwicklung eines Gitterspektrometers zur Untersuchung vakuumultravioletter Strahlung von hochgeladenen Ionen," 2008.

[21] "Nist atomic spectra database ionization energies form." https://physics.nist.gov/PhysRefData/ASD/lines_form.html. Accessed: 2018-07-10.

[22] Scofield ,J., "Ionization Energies," *LLNL Interner Report*, 1975.

[23] J. Jäger, "Untersuchung von metastabilen zuständen hochgeladener ruthenium-ionen mittels euv-spektroskopie," 2017.

[24] K. Palumbo, *Atomic and Ionic Emission Lines below 2000 Angstroms*. Washington, D.C: Nove Science Publishers, 1973.

[25] M. Gu, "The flexible atomic code," *Canadian Journal of Physics*, vol. 86, no. 5, pp. 675–689, 2008.

Acknowledgements

Here I like to thank all the people which have supported me in the process of this thesis.
Firstly, I like to thank Dr. José R. Crespo for supervising this thesis. Thank you for the special lab tour when I was visiting the group for the first time (this has really filled me with enthusiasm to join the group) and the detailed answers to all my questions. Thank you for writing me the letter of recommendation for the residence in Paris. I'm sure it was an important contribution for them accepting me.
Secondly, I want to thank Dr. Chintan Shah for all the patience with me. Thank you for always taking time to listen to my questions and problems and reassuring me. Thank you for helping me so much in the process of this thesis.
Besides, I would like to thank all the members of the group. Thank you for the warm welcome and all the little discussions during coffee and cake breaks. I was really enjoying the time at the institute. Thank you for all the interesting insides in your experiments. Particularly I have to thank you for all the support you have given me in the last days. Especially thanks to Stephan and Sven, Julian and Michael for your feedback during the writing process and all the comfort you have given me. Without you, this thesis wouldn't be what it is today. Thanks to Julia for giving me so much helpful advice.
Last I would like to thank Dr. Thomas Pfeifer for agreeing to be my second examiner and enable the colloquium scheduled at this date.

Erklärung

Ich versichere, dass ich diese Arbeit selbstständig verfasst und keine anderen als die angegebenen Quellen und Hilfsmittel benutzt habe.

Heidelberg, den 7. August 2018, ...